JOURNAL OF GEOPHYSICAL RESEARCH, VOL. 106, NO. D11, PAGES 11,977–11,995, JUNE 16, 2001

Aerosol properties derived from aircraft multiangle imaging over Monterey Bay

Ralph Kahn, Pranab Banerjee, Duncan McDonald, and John Martonchik
Jet Propulsion Laboratory, California Institute of Technology, Pasadena, California

Abstract. The first generic and climatological aerosol retrievals using AirMISR data are presented. Multiangle observations at 672 and 867 nm, in a cloud-free region over dark water in Monterey Bay on June 29, 1999, yield complementary generic and climatological results. The generic retrieval produces cross-section-weighted, column-mean aerosol properties: midvisible aerosol optical depth between 0.05 and 0.10, with a preference for values on the low side of the range, particle number-mean characteristic radius between 0.25 and 0.45 μm, and imaginary index of refraction <0.004, with 0.0 as the most likely value. These properties correspond to a "medium-to-large, spherical" column-average particle. The climatological retrieval identifies a maritime air mass, having a total aerosol optical depth about 0.1, and mixing ratio for sea-salt particles (large, spherical) of 50%, based on optical depth in MISR Band 2, and 40% for the sulfate plus carbonaceous (medium, spherical) components, to an accuracy of about $\pm 15\%$. These results are in good agreement with the limited nearby surface-based and aircraft observations available. The analysis also shows that over dark water, pixel-to-pixel scene variability can contribute more to the retrieval uncertainty than camera calibration and that high spatial variance of the reflectance, in addition to geometric considerations, is a better indicator of Sun glint contamination than geometry alone. This work represents an early step toward the goal of using MISR multiangle data to add spatial detail and information about temporal variability to the global aerosol climatology.

1. Introduction

The Multiangle Imaging Spectroradiometer (MISR) instrument was launched into polar orbit on December 18, 1999, aboard the Earth Observing System (EOS) Terra spacecraft, after years of preparation and anticipation. MISR measures upwelling radiance from Earth in four spectral bands centered at 446, 558, 672, and 867 nm, at each of nine view angles spread out in the forward and aft directions along the flight path, at $\pm 70.5°$, $\pm 60.0°$, $\pm 45.6°$, $\pm 26.1°$, and nadir [*Diner et al*., 1998a]. The spatial sampling rate is 275 m at all angles. Over a period of 7 min, as the spacecraft flies overhead, a 360 km wide swath of Earth is successively viewed by each of the cameras. MISR samples a very large range of scattering angles; in midlatitudes the instrument observes scattering angles between about 60° and 160°. Global coverage is acquired about once in nine days at the equator; the nominal mission lifetime is 6 years.

Surface, aerosol, and cloud properties are derived from MISR data. Since MISR is a new instrument, we are planning an extensive validation program to assess the sensitivity of the algorithms to aerosol properties under a variety of natural conditions. Quantitative measures of MISR aerosol product uncertainties will result, along with ideas for improving the algorithms themselves. The validation program encompasses a range of field measurements and coordinated campaigns. This paper, which presents the analysis of data from one of the first postcheckout flights of the AirMISR aircraft instrument, is an early step in the program.

A major science objective of the MISR program is to derive aerosol physical properties, in addition to optical depth, from the multiangle data. The MISR Team has developed standard algorithms to retrieve aerosol characteristics over dark water, dense dark vegetation, and heterogeneous land [*Martonchik et al*., 1998]. In addition to the standard aerosol retrieval algorithms, which are designed to run efficiently in a production mode, we developed several more flexible research algorithms, and explored their sensitivity using simulated MISR data [*Kahn et al*., 1997, 1998, 2000]. Their performance is expected to be best over dark water, where the surface contribution to the observed radiance is minimal, and for the MISR red and near-infrared (NIR) bands only, where the ocean surface is expected to be darkest. In this paper we apply both the generic and the climatological research algorithms to AirMISR data. We compare the results with each other, and with the limited nearby surface-based and aircraft observations available for this case.

The generic algorithm [*Kahn et al*., 1998] asks how well we can distinguish among particles having systematically and independently varying ranges of properties. It steps through a four-dimensional space, covering natural ranges of effective size, real and imaginary refractive indexes, and optical depth. This algorithm interprets top-of-atmosphere radiances in terms of a column-averaged, cross-section-weighted mean aerosol population. The retrieval produces aerosol physical properties assuming a monomodal, lognormal distribution of either spherical or randomly oriented nonspherical particles. For observations taken where a single-particle mode dominates, the generic retrieval is a powerful tool for constraining particle properties within the limits of the data. Even for multimodal situations the retrieval identifies ranges of column-averaged aerosol properties in four dimensions, an important

Paper number 2000JD900740.
0148-0227/01/2000JD900740$09.00

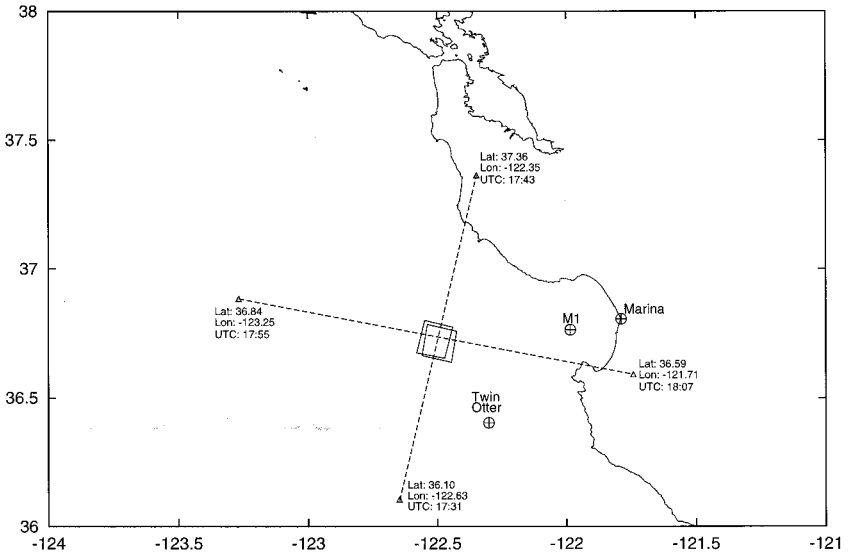

Figure 1. Map of the AirMISR Monterey Bay field site for June 29, 1999. Approximate flight lines for Runs 1 and 2 are indicated with dashed lines joining the end points, which are marked with triangles and labeled with latitude, longitude, and AirMISR crossing time (UTC). The locations of the nadir-looking images for Runs 1 and 2, which also correspond to the maximum overlap region for AirMISR data from all angles, are shown as rectangles along the flight lines. The location of the MISR team's Marina coastal field station is designated with a circled plus sign labeled Marina. The Monterey Bay Aquarium Research Institute operational buoy location (36°45′11″N latitude, 122°1′11″W longitude) is indicated with a circled plus sign labeled M1, and the location of the Twin Otter profiles is marked as well.

indication of the information content of observations. However, if the aerosol distribution is multimodal, the average column particle properties may not correspond to any individual particles present. This limitation is true of many satellite retrievals in current use, such as those that solve for aerosol optical depth and an "Angstrom coefficient," which amounts to assuming a monomodal distribution.

An alternative, climatological aerosol retrieval [*Kahn et al*., 2000], asks how well MISR can distinguish among assumed, climatologically probable mixtures of component particles. Climatological retrievals must assume a climatology of component particles and mixtures. The value of the climatological retrieval depends on quality of the assumed climatology. This means the assumed components should represent the particles in the column to within the sensitivity of the instrument. For example, since MISR is sensitive to about three size groupings across the natural range of aerosols for either spherical or randomly oriented nonspherical particles [*Kahn et al*., 1997, 1998], we can do no better than to select climatologically probable "small," "medium," and "large" components for each. (To obtain a more precise retrieval, we have to introduce data from other sources, if it is available.) The additional assumptions allow us to distinguish, as much as possible, multiple particle modes and air masses containing common mixtures of aerosols in Earth's atmosphere. In multimodal cases, climatological retrieval results are easier than generic retrieval results to compare with in situ observations and with aerosol transport model predictions.

AirMISR was built in preparation for the flight of MISR [*Diner et al*., 1998b]. It is intended both to provide data for testing MISR algorithms and, as a central part of the long-term MISR calibration and validation program, for the duration of the MISR mission. AirMISR was constructed from a single MISR brassboard camera and has nearly the same spectral and radiometric characteristics as the MISR cameras [*Chrien et al*., 1999]. Mounted on a motorized pivot, the AirMISR camera can be preprogrammed to image Earth at view angles encompassing $\pm 70.5°$ from nadir along the aircraft flight direction. The instrument flies in the nose of the NASA ER-2 high-altitude aircraft, at an elevation of about 20 km above sea level.

Engineering checkout flights for AirMISR were completed in spring 1999. On June 29, 1999, AirMISR acquired its first cloud-free, dark water science sequences over Monterey Bay. These observations represent our first opportunity to test the performance of the research aerosol retrieval algorithms with real data. The next sections explain how AirMISR data are processed into band-corrected equivalent reflectances needed for the aerosol retrievals and how simulated data are generated and compared with the measurements. The following sections present the generic and climatological retrieval results for the Monterey experiment. The final section places these results into a larger context and provides conclusions.

2. AirMISR Data

This section gives a brief summary of the AirMISR data used for this study and the processing steps we applied to obtain equivalent reflectance from the standard L1B2 product. The AirMISR data used in this study were acquired on Tuesday, June 29, 1999, over Monterey Bay, California, between 1030 and 1105 LT. Run 1 trended roughly northward, close to the ground track for the EOS spacecraft; the flight line for Run 2 headed eastward, toward the Sun, approximately orthogonal to Run 1. Figure 1 is a map of the Monterey coast, indicating the locations of these flight lines and of the nadir images for both runs, and Figure 2 is a gray-scale rendition of the nadir image for Run 1. Table 1 gives the corner locations and timing of the images.

For nominal flight conditions, AirMISR pixels cover an area at the surface 7 m cross track by 6 m along track when viewing in the nadir position; the coverage increases to 21 m cross track by 55 m along track when viewing at ±70.5°. A standard AirMISR viewing sequence has the camera dwelling first in the D-forward (Df) MISR viewing position (70.5°), and then successively stepping through the Cf (60°), Bf (45.6°), Af (26.1°), An (nadir), A-aft (Aa), Ba, Ca, and Da angles during a 12 min, 147 km ER-2 flight line. This sequence is timed so that overlap occurs for all nine viewing positions over the entire An image area, 11 km cross track by 9 km along track. Since the camera acquires push-broom data with lines centered every 8 m on the surface, the lines overlap considerably for the steeper viewing positions. The AirMISR Level 1B2 (L1B2) processing software resamples the images for all viewing positions to a uniform grid of 27.5 m pixels (one tenth of a MISR pixel). For a given viewing position, values assigned to each L1B2 pixel are the arithmetic means of all measurements at that viewing angle whose centers fall within the 27.5 m cell.

Level 1 AirMISR geometric, radiometric, and spectral calibration processing follows closely the procedures established for handling MISR data [*Bruegge et al*., 1999a, 1999b, 1998a; *Jovanovic et al*., 1998]. The key data products for the current study are the AirMISR Monterey 1999 June 29 Runs 1 and 2 standard L1B2 data files. These and other AirMISR and MISR data are archived in the EOS extension of Hierarchical Data Format (HDF-EOS) and are distributed by the Atmospheric Sciences Data Center at the NASA Langley Research Center.

The AirMISR L1B2 images have been corrected for any dropped lines using linear interpolation. (For the data set used here, only three of the eighteen 1000 line data sets had interpolated lines; Bf NIR, 1 line; Af red, 2 lines; and Af NIR, 10 lines.) Some adjustment is made for airplane roll and pitch errors based on the inertial navigation system (INS) derived aircraft navigation file. However, as illustrated by the wavy contours in Figure 3a, small changes in aircraft pitch still alter the view zenith angle by several degrees. Figure 3 also illustrates how view azimuth varies by 60° over the AirMISR Aa image, since AirMISR flies only about 20 km above the ground. Because of the 704 km elevation and relatively stable spacecraft platform on which MISR flies, both small-scale fluctuations and overall variations in viewing geometry across MISR images are orders of magnitude smaller than those for AirMISR.

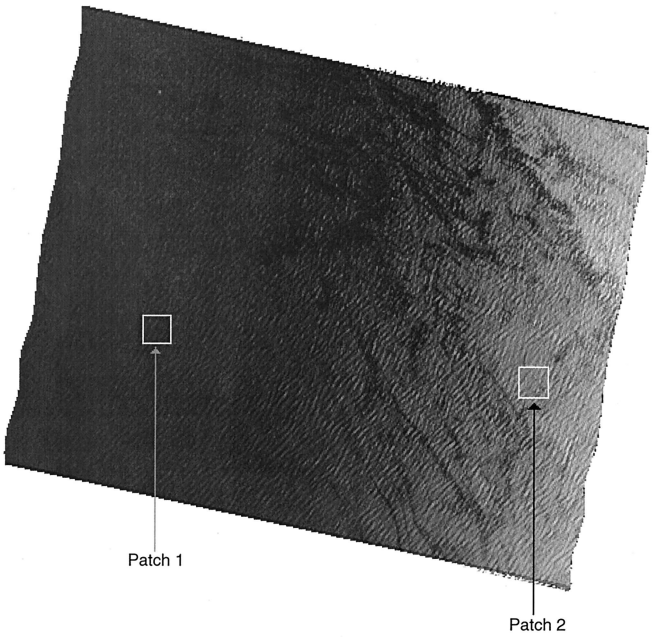

Figure 2. Gray-scale versions of the L1B2 AirMISR An (nadir looking) images for Monterey Bay, June 29, 1999, Run 1. North is toward the top of the page. For this image the green AirMISR data were assigned to the blue image plane, the red AirMISR data were set to green, and the near-IR data were displayed as red, then the aggregate was reproduced as a gray-scale image. The image is highly stretched and would appear dark and uniform without enhancement. The locations of the 21 by 21 pixel study patches are indicated with squares. The patch coordinates are given in Table 1.

Table 1. AirMISR Nadir Image Corner and Patch Locations

Latitude	Longitude	Image Sample[a] (x)	Image Line[a] (y)
Run 1, Start Time, 1731:12 UTC			
36°46.56′	−122°32.22′	587	662
36°40.56′	−122°33.9′	534	990
36°39.54′	−122°27.96′	937	1079
36°45.54′	−122°26.28′	992	749
Patch corners			
run 1 patch 1	upper left	654	875
run 1 patch 1	lower right	674	895
run 1 patch 2	upper left	897	910
run 1 patch 2	lower right	917	930
Run 2, Start Time, 1755:07 UTC			
36°45.96′	−122°31.47′	510	470
36°39.88′	−122°32.84′	438	879
36°38.96′	−122°26.77′	767	939
36°45.04′	−122°25.32′	838	530
Patch corners			
run 2 patch 1	upper left	600	650
run 2 patch 1	lower right	620	670

[a]L1B2 data are geometrically calibrated and coregistered, so image line and sample numbers correspond to the same geographic locations, within calibration uncertainty, for images from a given run taken at all look angles.

For AirMISR analysis we select patches 21 by 21 pixels (578 m by 578 m) in size, over which the viewing geometry and radiance patterns are fairly uniform. Two white squares in Figure 2 locate two of the three main patches used for this study. (The third patch was selected in the Run 2 data.) Also visible in this highly stretched image is a pattern of streaks running parallel to the line of flight. This pattern is more pronounced in the images taken at steeper viewing angles, but it shows up only for low-contrast targets such as the ocean surface; it is a small effect, usually amounting to less than 2% (always less than 5%) differences in the mean reflectance. The MISR and AirMISR cameras each contain four line arrays of 1504 active pixels, one line for each color band. An image is built up as the line arrays, which are oriented cross track, are carried along track by the motion of the instrument. The streak pattern arises from tiny variations in pixel-to-pixel calibration.

The standard AirMISR L1B2 product includes a band-and-camera specific, pixel-by-pixel Data Quality Indicator (DQI), which is set to zero for usable data, and to 255 if a flag is set at any step in the Level 1 processing. (For the standard MISR L1B2 product, there are separate radiometric and geometric data quality indicators.) We include only pixels with DQI = 0

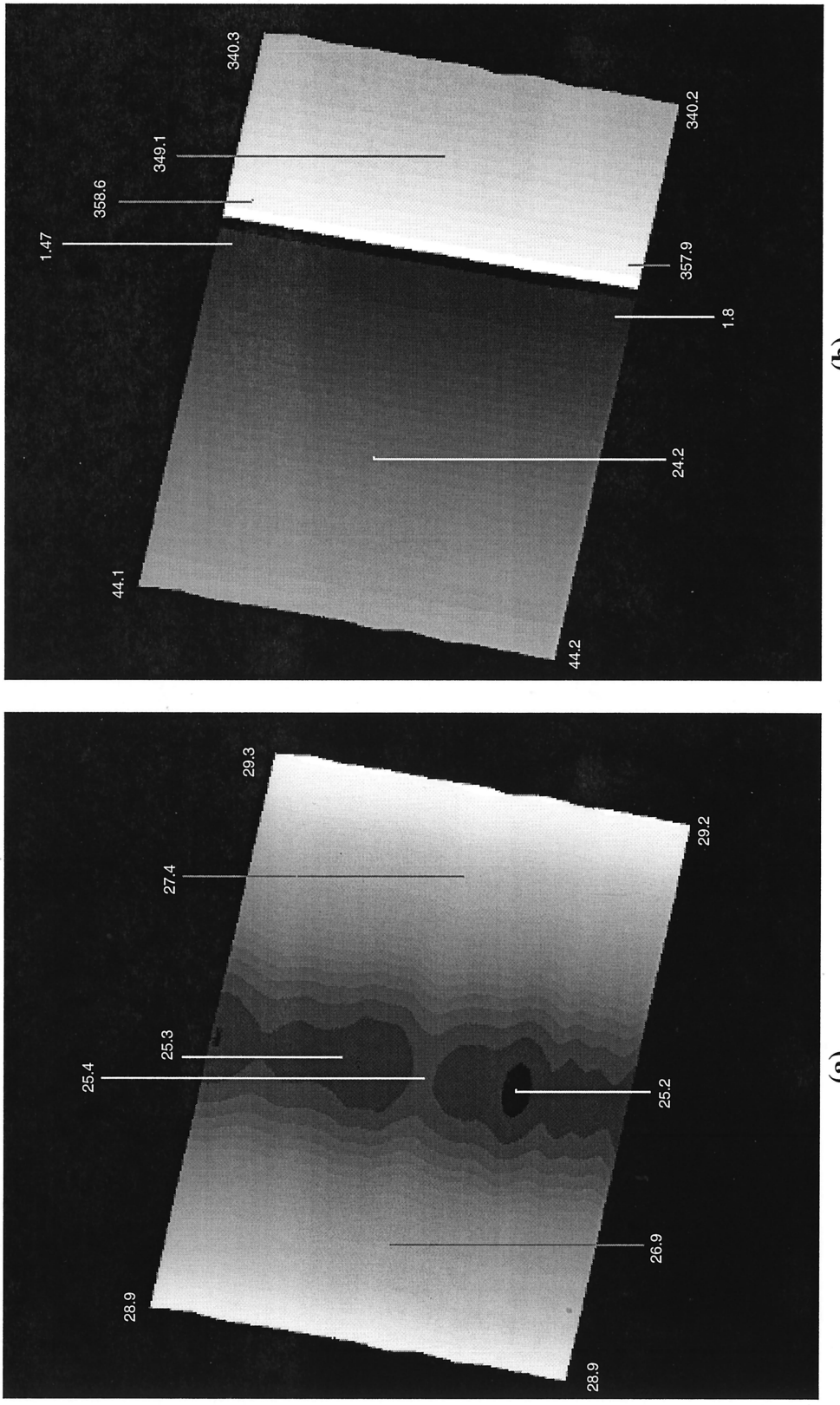

Figure 3. Viewing geometry of the Aa camera position for Run 1, AirMISR Monterey flight, June 29, 1999. These highly stretched gray-scale images show (a) view zenith and (b) view azimuth angles. The zenith angle values are around 25° in the darkest areas and about 29° in the lightest areas, whereas the azimuth angle ranges from values near 40° along the left edge, crossing the 0°/360° line, down to values near 340° along the right edge of the image.

Table 2. Monterey Bay AirMISR Geometry Data, June 29, 1999[a]

Look Angle	Sun Zenith	Sun Azimuth	View Zenith	View Azimuth	Sun Glint Angle
			Run 1 Patch 1		
Df	37.32	279.6	72.80	188.1	77.29
	(0.002)	(0.004)	(0.019)	(0.14)	
Cf	36.86	280.1	61.24	186.4	69.45
	(0.003)	(0.004)	(0.025)	(0.25)	
Bf	36.62	280.3	47.26	183.9	60.27
	(0.003)	(0.005)	(0.037)	(0.42)	
Af	36.45	280.5	28.89	178.0	50.05
	(0.003)	(0.005)	(0.090)	(0.80)	
An	36.27	280.7	6.706	111.3	42.88
	(0.003)	(0.005)	(0.442)	(0.65)	
Aa	36.11	280.8	25.76	23.94	47.98
	(0.003)	(0.005)	(0.073)	(0.92)	
Ba	35.93	281.0	44.75	16.85	57.79
	(0.003)	(0.005)	(0.026)	(0.46)	
Ca	35.70	281.3	59.27	14.09	67.01
	(0.003)	(0.005)	(0.007)	(0.27)	
Da	35.37	281.6	69.58	12.62	74.05
	(0.004)	(0.007)	(0.031)	(0.17)	
			Run 1 Patch 2		
Df	37.24	279.7	72.64	194.0	73.69
	(0.004)	(0.006)	(0.021)	(0.15)	
Cf	36.80	280.1	61.22	196.7	63.52
	(0.003)	(0.005)	(0.012)	(0.25)	
Bf	36.56	280.4	47.39	201.1	51.30
	(0.003)	(0.005)	(0.038)	(0.42)	
Af	36.38	280.5	29.36	211.5	36.29
	(0.003)	(0.005)	(0.117)	(0.77)	
An	36.21	280.7	11.56	277.6	24.67
	(0.003)	(0.005)	(0.434)	(0.20)	
Aa	36.04	280.9	27.70	347.3	34.37
	(0.003)	(0.005)	(0.157)	(0.78)	
Ba	35.87	281.1	45.56	358.6	48.86
	(0.003)	(0.006)	(0.065)	(0.43)	
Ca	35.63	281.3	59.61	3.267	61.22
	(0.003)	(0.005)	(0.021)	(0.263)	
Da	35.29	281.7	69.93	5.859	70.41
	(0.007)	(0.009)	(0.092)	(0.165)	
			Run 2 Patch 1		
Df	32.59	284.7	71.71	280.4	39.25
	(0.003)	(0.004)	(0.0273)	(0.15)	
Cf	32.20	285.1	61.20	279.3	29.28
	(0.005)	(0.006)	(0.0415)	(0.25)	
Bf	32.20	285.4	46.79	278.2	15.51
	(0.005)	(0.005)	(0.0260)	(0.43)	
Af	31.77	285.7	27.21	275.6	6.73
	(0.004)	(0.005)	(0.0276)	(0.88)	
An	31.61	285.9	2.77	209.3	31.07
	(0.004)	(0.005)	(0.4248)	(3.16)	
Aa	31.44	286.1	25.41	106.3	56.85
	(0.004)	(0.005)	(0.0413)	(0.95)	
Ba	31.27	286.3	45.03	103.4	76.27
	(0.004)	(0.005)	(0.0201)	(0.45)	
Ca	31.04	286.6	59.41	102.3	90.38
	(0.004)	(0.005)	(0.0080)	(0.27)	
Da	30.67	287.1	70.38	101.7	100.93
	(0.004)	(0.006)	(0.0048)	(0.16)	

[a]Columns 2–5 are averages over 441-pixel patches. Numbers in parentheses are standard deviations. All angles are in degrees.

in the AirMISR analysis. For the Monterey experiment data used, all pixels meet this criterion.

Table 2 contains the mean and standard deviation values for the view zenith and azimuth, as well as the Sun zenith and azimuth, at each of the nine look angles, for all three patches. Viewing down toward Earth, azimuth is measured clockwise from north, for the vector pointing in the direction of photon travel (which resolves the 180° ambiguity in vector definition). In all cases the geometry varies much less than 1° over a patch. Column 6 gives the Sun glint angle (ζ), defined as

$$\zeta = \cos^{-1}\{\cos(\theta_0)\cos(\theta) + \sin(\theta_0)\sin(\theta)\cos(\phi_0 - \phi)\}. \quad (1)$$

Here θ_0 is the Sun zenith angle, θ is the view zenith angle, and ϕ_0 and ϕ are the Sun and view azimuth angles, respectively.

When ζ is small, the camera is looking in a direction near that of the Sun's specular reflection, and the data may be contaminated. The size of the region affected by Sun glint depends on surface type, and for ocean, it also depends on wind speed, wind azimuth, and Sun position relative to the viewing direction. In the AirMISR observations used here, the standard deviations for data having ζ below 30° or 40° are relatively large, indicating possible contamination; a Sun glint mask allows us to eliminate contaminated pixels from the analysis.

Radiometry data for the three patches are given in Table 3. Columns 2 through 5 contain the mean and standard deviation values of the spectral DNs for each look angle and patch, as extracted from the AirMISR L1B2 product. (Note that the "DNs" in the L1B2 product are not the original instrument DNs; they are integer representations of radiometrically calibrated and scaled, geometrically resampled radiances derived by MISR L1B1 and L1B2 processing.) The spectral equivalent reflectances are calculated according to

$$\rho(l, k) = L(l, k) \times \pi \times D^2/E_0, \tag{2a}$$

$$\sigma_\rho(l, k) = \Delta L(l, k) \times \pi \times D^2/E_0. \tag{2b}$$

Here indices l and k are for band and view angle, respectively. $L(l, k)$ and $\Delta L(l, k)$ are the radiance and radiance standard deviation, respectively, for the look angle and band, averaged over all the pixels in the patch of interest. They are calculated by multiplying the patch-mean L1B2 data number ($DN(l, k)$) and its standard deviation ($\Delta DN(l, k)$) by a band-specific radiometric scale factor (called Rad_scale_factor in the AirMISR and MISR products). (Note that for the MISR but not the AirMISR L1B2 products, the reported DNs must be divided by 4.0 and then truncated to integers, to remove a two bit data quality indicator encoded in the data and to obtain the scaled radiance DNs.) In (2a) and (2b), D is the Earth-Sun distance in AU, and E_0 is the band-specific solar irradiance at 1 AU, which is called std_solar_wgted_height, and is stored, along with all the other factors needed, as "grid metadata" in the standard AirMISR L1B2 product.

Part of the radiometric calibration involves correcting the reported radiances in each band for sensitivity to light at wavelengths outside the intended passband. For a solar-spectrum-weighted signal, the AirMISR red band has a 4.92% out-of-band sensitivity, coming primarily from blue light. This is about 2.5 times the out-of-band sensitivity for the spacecraft MISR red band and nearly twice the out-of-band sensitivity of any other band on either the MISR or the AirMISR instruments [*Chrien et al*., 1999]. Columns 6–9 of Table 3 contain band-corrected and ozone-corrected equivalent reflectances, along with estimates of the standard deviation. The band correction is calculated separately for each look angle, by multiplying the vector of four spectral equivalent reflectances obtained from (2a) for a given look angle by a correction matrix:

$$[\rho_{\text{corr}}] = [[\text{C}]] \times [\rho] \tag{3}$$

The terms in each row of the correction matrix C sum to 1, and the off-diagonal terms are 2 or 3 orders of magnitude smaller than the diagonal terms. The matrix C is given in the grid metadata of the AirMISR L1B2 product, as spectral_corr_matrix.

A correction is then made to the equivalent reflectance in each band for absorption by stratospheric ozone. The ozone optical depth is

$$\tau_{\text{ozone}}(l) = c_l D_{\text{ozone}} \tag{4a}$$

where c_l is a band-specific constant, equal to 4.26×10^{-6}, 1.05×10^{-4}, 5.09×10^{-5}, and 3.94×10^{-6} for MISR bands 1–4, respectively, and D_{ozone} is the ozone column amount in Dobson units [*Diner et al*., 1999a]. The ozone-corrected equivalent reflectance for spacecraft MISR measurements is

$$\rho(l, k)_{\text{ozone-corrected}} = \rho_{\text{corr}}(l, k) \cdot \exp\left[\tau_{\text{ozone}}\left(\frac{1}{\cos(\theta_0)} + \frac{1}{\cos(\theta)}\right)\right]. \tag{4b}$$

Since AirMISR flies below the stratospheric ozone layer, the cos (θ) term in (4b) is eliminated, and the correction for AirMISR is independent of view angle. The ozone correction is largest in band 2 but still amounts to no more than half the Rayleigh optical depth in that band, even when the ozone column is as high as 450 Dobsons. We use the band- and ozone-corrected equivalent reflectances in the AirMISR analysis, with an ozone column of 320 Dobsons, for the Monterey Bay experiment.

3. Modeling MISR Radiances and Comparing With Observations

This section discusses the tools we use to interpret MISR and AirMISR observations in terms of aerosol characteristics.

3.1. MISR Simulation Radiative Transfer Model

The MISR Team has developed a radiative transfer code that simulates reflectances as would be observed by MISR for an arbitrary choice of aerosol mixture, amount, and vertical distribution, variable surface reflectance properties, and user-selected Sun and viewing geometry [*Diner et al*., 1999b; *Martonchik et al*., 1998]. It is based on the matrix operator method [*Grant and Hunt*, 1968]. Radiances for mixtures of component aerosols are obtained by combining radiances for the individual components, weighted by fractional contribution to optical depth, according to the modified linear mixing method of *Abdou et al*. [1997].

For the present study we run the model to simulate MISR measurements over a Fresnel-reflecting ocean surface, in a cloud-free, Rayleigh-scattering atmosphere with 1.013 bar surface pressure, a standard midlatitude temperature profile, and aerosols (except transported accumulation mode dust) concentrated in a near-surface layer. A correction is made to the MISR band most affected by water vapor, Band 4 (at 867 nm), based on a typical midlatitude profile containing about 1.4 precipitable centimeters of water [*Diner et al*., 1999b]. It amounts to a band-averaged absorption optical depth of 0.002, which is small compared even to 0.016, the standard atmosphere Rayleigh-scattering optical depth for Band 4, and is negligible compared to anticipated MISR sensitivity to aerosol optical depth, of 0.05 or 20%, whichever is larger [*Kahn et al*., 1998].

The ocean surface boundary condition models whitecaps and Sun glint, using standard approaches that depend on near-surface wind speed. Since we use only MISR red and NIR channels for dark water aerosol retrievals, a third component of ocean surface reflection, arising from underlight, is so small it can be ignored [*Wang and Gordon*, 1994]. The bidirectional reflectance factor (BRF) is the surface-leaving radiance divided by the radiance from a Lambert reflector with the same

Table 3. Monterey Bay AirMISR L1B2 Radiometry Data, June 29, 1999[a]

Look Angle	Blue DN	Green DN	Red DN	NIR DN	Blue BCR	Green BCR	Red BCR	NIR BCR
				Run 1 Patch 1				
Df	2140	1074	605	345	0.1767	0.0915	0.0487	0.0278
	(10)	(5)	(5)	(9)	(0.0008)	(0.0004)	(0.0004)	(0.0007)
Cf	1618	763	390	201	0.1336	0.0650	0.0311	0.0160
	(6)	(3)	(4)	(2)	(0.0005)	(0.0003)	(0.0003)	(0.0002)
Bf	1329	609	286	141	0.1098	0.0519	0.0226	0.0112
	(6)	(2)	(2)	(1)	(0.0005)	(0.0002)	(0.0002)	(0.0001)
Af	1206	555	261	133	0.0996	0.0473	0.0206	0.0106
	(4)	(4)	(4)	(4)	(0.0003)	(0.0003)	(0.0003)	(0.0003)
An	1181	555	272	151	0.0975	0.0473	0.0216	0.0121
	(8)	(7)	(7)	(7)	(0.0007)	(0.0006)	(0.0006)	(0.0006)
Aa	1188	541	251	127	0.0981	0.0461	0.0198	0.0101
	(5)	(3)	(2)	(2)	(0.0004)	(0.0003)	(0.0002)	(0.0002)
Ba	1283	581	269	130	0.1060	0.0495	0.0212	0.0103
	(6)	(3)	(2)	(1)	(0.0005)	(0.0003)	(0.0002)	(0.0001)
Ca	1552	707	348	171	0.1282	0.0602	0.0276	0.0136
	(5)	(4)	(3)	(2)	(0.0004)	(0.0003)	(0.0002)	(0.0002)
Da	1999	949	509	260	0.1651	0.0808	0.0407	0.0208
	(10)	(5)	(4)	(3)	(0.0008)	(0.0004)	(0.0003)	(0.0002)
				Run 1 Patch 2				
Df	2087	1072	628	347	0.1723	0.0914	0.0507	0.0279
	(8)	(8)	(6)	(4)	(0.0007)	(0.0007)	(0.0005)	(0.0003)
Cf	1590	754	385	207	0.1313	0.0642	0.0307	0.0165
	(6)	(2)	(2)	(1)	(0.0005)	(0.0002)	(0.0002)	(0.0001)
Bf	1273	586	280	145	0.1052	0.0499	0.0222	0.0115
	(5)	(2)	(3)	(1)	(0.0004)	(0.0002)	(0.0002)	(0.0001)
Af	1119	523	255	143	0.0924	0.0446	0.0202	0.0114
	(8)	(8)	(8)	(8)	(0.0007)	(0.0007)	(0.0007)	(0.0007)
An	1249	742	508	422	0.1030	0.0632	0.0416	0.0346
	(70)	(86)	(95)	(104)	(0.0057)	(0.0070)	(0.0078)	(0.0086)
Aa	1094	508	241	131	0.0904	0.0433	0.0191	0.0104
	(5)	(3)	(3)	(3)	(0.0004)	(0.0003)	(0.0002)	(0.0002)
Ba	1241	570	270	137	0.1025	0.0485	0.0213	0.0109
	(5)	(3)	(3)	(1)	(0.0004)	(0.0003)	(0.0002)	(0.0001)
Ca	1554	729	369	190	0.1283	0.0621	0.0294	0.0151
	(6)	(3)	(4)	(2)	(0.0005)	(0.0003)	(0.0003)	(0.0002)
Da	2070	1017	561	301	0.1709	0.0866	0.0450	0.0241
	(12)	(10)	(8)	(5)	(0.0010)	(0.0009)	(0.0007)	(0.0004)
				Run 2 Patch 1				
Df	2280	1330	891	636	0.1880	0.1129	0.0726	0.0519
	(10)	(11)	(15)	(17)	(0.0008)	(0.0009)	(0.0013)	(0.0014)
Cf	1709	1018	708	569	0.1409	0.0864	0.0578	0.0466
	(34)	(45)	(56)	(59)	(0.0028)	(0.0038)	(0.0047)	(0.0049)
Bf	2062	1767	1611	1586	0.1694	0.1499	0.1339	0.1310
	(168)	(208)	(224)	(246)	(0.0137)	(0.0176)	(0.0188)	(0.0204)
Af	2890	2862	2864	2952	0.2370	0.2427	0.2391	0.2443
	(247)	(296)	(327)	(327)	(0.0202)	(0.0251)	(0.0274)	(0.0294)
An	1252	657	389	282	0.1033	0.0558	0.0314	0.0229
	(40)	(48)	(54)	(58)	(0.0033)	(0.0041)	(0.0045)	(0.0048)
Aa	1434	653	314	153	0.1184	0.0554	0.0248	0.0121
	(3)	(4)	(4)	(3)	(0.0002)	(0.0003)	(0.0003)	(0.0002)
Ba	1751	797	401	195	0.1446	0.0676	0.0317	0.0155
	(4)	(4)	(4)	(2)	(0.0003)	(0.0003)	(0.0003)	(0.0002)
Ca	2168	990	517	247	0.1790	0.0840	0.0411	0.0196
	(6)	(5)	(4)	(3)	(0.0005)	(0.0004)	(0.0003)	(0.0002)
Da	2782	1316	732	357	0.2297	0.1116	0.0585	0.0285
	(7)	(4)	(5)	(4)	(0.0006)	(0.0003)	(0.0004)	(0.0003)

[a]These data are averaged values over 441-pixel patches. Numbers in parentheses are standard deviations. Band- and ozone-corrected equivalent reflectances (BCR, columns 6–9) are calculated using equations (3) and (4). The band-specific radiometric scale factors (Rad_scale_factor) used for this case: 0.04720 (blue), 0.04653 (green), 0.03853 (red), and 0.02467 (NIR). The band-specific standard solar irradiance (std_inband_solar_wgted_height) used: 1872.20430 (blue), 1850.03590 (green), 1524.45570 (red), and 969.84381 (NIR). The Earth-Sun distance is 1.016607 for June 29, 1999, and the ozone correction applied here is for a column abundance of 320 Dobsons.

illumination ($= \rho/\cos\theta_0$). The BRF for the ocean surface due to whitecaps (in the absence of diffuse skylight) is given by the empirical relationship:

$$R^{\text{whitecap}} = 0.22 \times 2.95 \times 10^{-6} \times W^{3.52}, \quad (5)$$

where W is the wind speed in m s^{-1}, measured 10 m above the surface. This commonly used relationship combines an equation describing the wind-speed-dependent area covered with whitecaps [*Monahan and Muircheartaigh*, 1980], with an average albedo of 22% for whitecap patches [*Koepke*, 1984].

Equation (5) applies at visible wavelengths shorter than about 900 nm, for wind speeds less than about 18 m s^{-1}, and is thought to be accurate to 20 or 30%, depending on unmodeled local conditions [*Koepke*, 1984]. The result is a wavelength-independent, Lambert contribution to the hemispherical albedo from whitecaps, with values 0.0002, 0.002, and 0.009 for surface wind speeds of 5, 10, and 15 m s^{-1}, respectively. For comparison the standard AVHRR satellite aerosol retrieval algorithm assumes the ocean to be a Lambert surface with hemispherical albedo 0.002 at 630 nm wavelength [*Stowe et al*., 1997].

The glitter model is based on the popular semiempirical relationship between near-surface wind speed (W) in m s^{-1}, and the probable distribution of mean squared ocean surface facet slopes (s^2) of *Cox and Munk* [1954]:

$$2s^2 = 0.003 + 0.0512 \times W. \tag{6}$$

This model assumes some fluctuation of the ocean surface even at zero wind speed. A theoretical ocean surface BRF is obtained by combining (6) with the Fresnel reflection equations appropriate to the air-water interface, and with a wave-shadowing function derived by *Tsang et al*. [1985]. The result has been applied to a case that includes polarization [*Mishchenko and Travis*, 1997] and to the scalar situation that accounts only for intensity, as is appropriate to MISR and AirMISR data [*Martonchik et al*., 1998]. Figure 4 shows the glitter component of the assumed ocean BRF for Sun zenith angle 33°, and all view zenith and azimuth angles in the upward looking hemisphere, for wind speeds of 0, 2.5, 5, and 10 m s^{-1}.

3.2. Testing Agreement Between Measurements and Comparison Models

Equivalent reflectances at the MISR angles and bands are generated by the radiative transfer model, for atmospheres containing different aerosol amounts, sizes, shapes, and compositions. The 18 values corresponding to the nine MISR angles in the red and NIR channels used for ocean aerosol retrievals are then compared to the AirMISR measurements. We define four test variables to decide whether a comparison model is consistent with the measurements [*Kahn et al*., 1998, 2000]. Each is based on the χ^2 statistical formalism [e.g., *Bevington and Robinson*, 1992].

One test variable weights the contributions from each observed reflectance according to the slant path through the atmosphere of the observation:

$$\chi^2_{\text{abs}} = \frac{1}{N\langle w_k\rangle} \sum_{l=3}^{4} \sum_{k=1}^{9} \frac{w_k[\rho_{\text{meas}}(l,k) - \rho_{\text{comp}}(l,k)]^2}{(\sigma^2_{\text{abs.cal}}(l,k;\rho_{\text{meas}}) + \sigma^2_{\text{abs.var}}(l,k))}, \tag{7a}$$

where ρ_{meas} is the measured equivalent reflectance, and ρ_{comp} is the simulated equivalent reflectance for the comparison model; l and k are the indices for wavelength band and look angle, N is the number of measurements included in the calculation, w_k are weights, chosen to be the inverse of the cosine of the view angle appropriate to each look angle k, $\langle w_k\rangle$ is the average of weights for all the measurements included in the summation, and $\sigma_{\text{abs}}(l, k; \rho_{\text{meas}})$ is the absolute calibration uncertainty in equivalent reflectance for AirMISR band l and look angle k. We model the measurement uncertainty as the sum of two independent terms, one due to calibration uncertainty ($\sigma_{\text{abs.cal}}$), the other to the pixel-to-pixel variance over the patch ($\sigma_{\text{abs.var}}$).

Value $\sigma_{\text{abs.cal}}$ varies with equivalent reflectance. It consists of a term produced by systematic uncertainty, $\varepsilon_{\text{abs\_sys}}$, which is reported as a percent in the standard MISR and AirMISR products, and a second term arising from random error, related to the inverse of the signal-to-noise ratio (SNR) [*Bruegge et al*., 1998b]. The SNR_{am} depends on the "averaging mode," i.e., the number of MISR or AirMISR pixels averaged to produce the measured DNs. (For MISR global observations the averaging mode is 4 × 4 pixels. For AirMISR L1B2 data the number of acquired pixels averaged to produce an image pixel varies with viewing geometry, but since the signal-to-noise ratio is so large, no error is introduced by using the values appropriate to 4 × 4 averaging.) The equation for the absolute calibration uncertainty is

$$\sigma^2_{\text{abs.cal}}(l,k) = \rho^2_{\text{meas}}[(\varepsilon_{\text{abs\_sys}}(l,k;\rho_{\text{meas}})/100)^2 + (\text{SNR}_{am}(l,k;\rho_{\text{meas}}))^{-2}]. \tag{7b}$$

Although $\varepsilon_{\text{abs\_sys}}$ can vary with l, k, and ρ_{meas}, the early assessment made of the calibration error budget produced a value of 1.6 for all cases [*Bruegge et al*., 1998b]. Even for dark water scenes, the AirMISR and MISR cameras exhibit high signal-to-noise ratios. For equivalent reflectances of 0.01 the smallest values found in this study (Table 3), the first term in brackets in (7b) is still at least an order of magnitude larger than the second term. (For this reason, the SNR term was ignored in sensitivity studies based on simulations of MISR data [*Kahn et al*., 1997, 1998, 2000].)

Value $\sigma^2_{\text{abs.var}}(l, k)$ is the variance of equivalent reflectance calculated for all the pixels in a patch:

$$\sigma^2_{\text{abs.var}}(l,k) = \frac{1}{M} \sum_j [\rho_{\text{meas}}(j;l,k) - \langle\rho_{\text{meas}}(l,k)\rangle]^2, \tag{7c}$$

where j is the index designating pixels in the patch, M is the total number of pixels in the patch, and $\langle\rho_{\text{meas}}(l, k)\rangle$ is the measured reflectance in band l and view angle k, averaged over all pixels in the patch. Depending on the scale of the variations, some or the whole SNR term in (7b) may be included in the pixel-to-pixel variance given by (7c). However, we do not have the data to address this issue, and SNR is so small relative to the other terms for the data used in this paper that the ambiguity does not affect the results. Values of $\sigma^2_{\text{abs.cal}}$ as a whole are of the order of 10^{-7}–10^{-8} for data uncontaminated by Sun glint, as are values of $\sigma^2_{\text{abs.var}}$ (Table 3). In both cases the uncertainty amounts to a few percent of the measurement.

χ^2_{abs} alone reduces 18 measurements to a single statistic. χ^2_{abs} emphasizes the absolute reflectance, which depends heavily on aerosol optical depth for bright aerosols over a dark surface. However, there is more information in the measurements that we can use to improve the retrieval discrimination ability. A second χ^2 test variable emphasizes the geometric properties of aerosol scattering, which depend heavily upon particle size and shape. For the χ^2_{geom} test variable, each spectral measurement is divided by the corresponding spectral measurement in one look direction, which we usually take as the nadir view:

$$\chi^2_{\text{geom}} = \frac{1}{N\langle w_k\rangle} \sum_{l=3}^{4} \sum_{\substack{k=1 \\ k\neq\text{nadir}}}^{9} \frac{w_k\left[\dfrac{\rho_{\text{meas}}(l,k)}{\rho_{\text{meas}}(l,\text{nadir})} - \dfrac{\rho_{\text{comp}}(l,k)}{\rho_{\text{comp}}(l,\text{nadir})}\right]^2}{(\sigma^2_{\text{geom.cal}}(l,k;\rho_{\text{meas}}) + \sigma^2_{\text{geom.var}}(l,k))}. \tag{8a}$$

The denominator in the sum is the uncertainty in angle-to-angle equivalent reflectance ratio appropriate to view angle k,

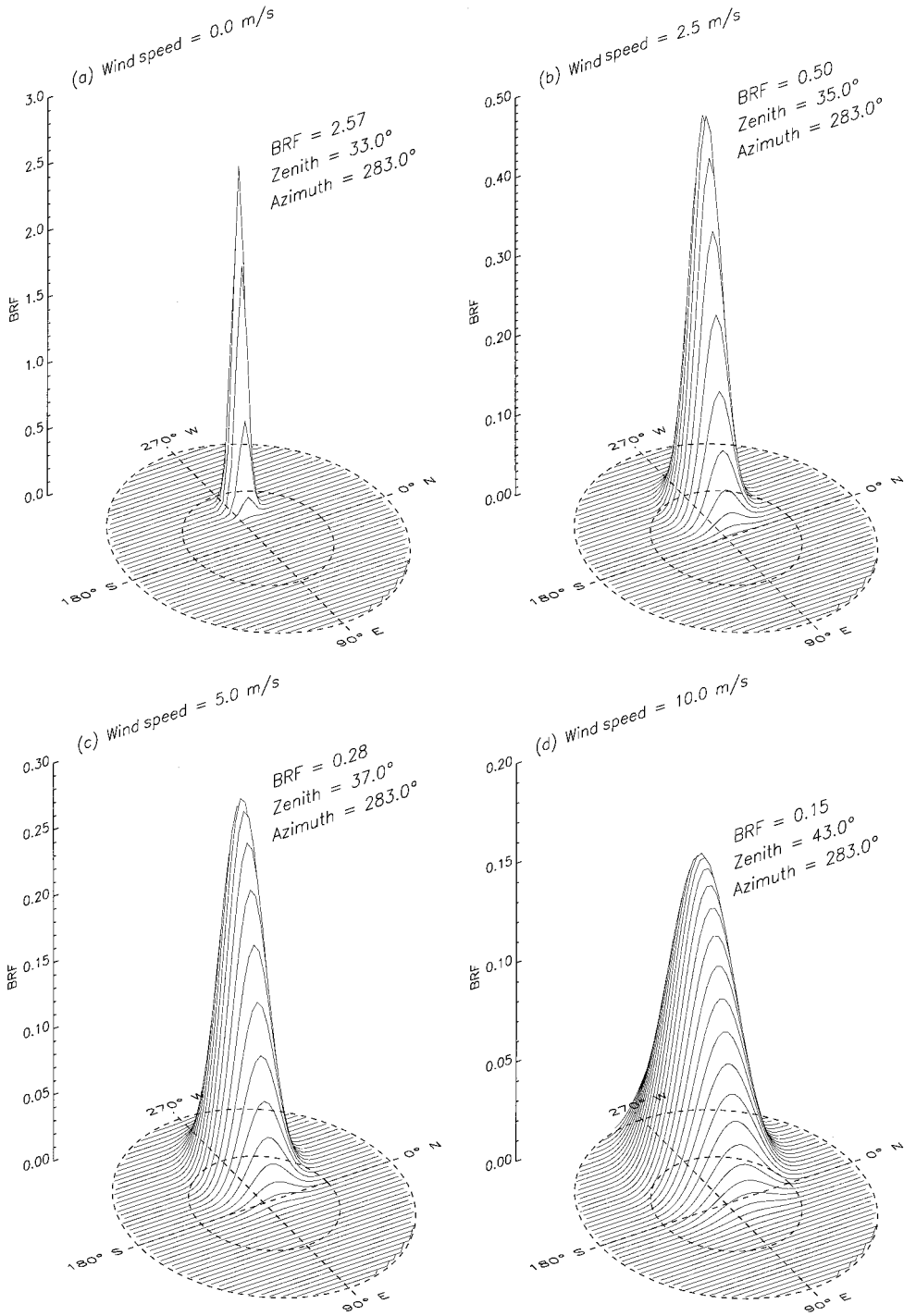

Figure 4. Model bidirectional reflection factors (BRFs) for the component of the ocean surface boundary condition due to glitter, with Sun zenith angle 33° and Sun azimuth 283°, at near-surface wind speed: (a) zero, (b) 2.5, (c) 5, and (d) 10 m s^{-1}. View zenith and azimuth angles at the peak of each distribution are given, along with the relative value of the BRF at that point, on a linear scale having value zero at the base. The inner and outer dashed circles indicate view zenith angles of 45° and 90°, respectively.

band l, and the equivalent reflectance measured by AirMISR. It is modeled as the sum of a calibration term and a contribution from pixel-to-pixel variance. Value $\sigma^2_{\text{geom.cal}}$ is derived from the expansion of errors for a ratio of measurements ($\sigma^2(f(x, y)) = (\partial f/\partial x)^2\sigma_x^2 + (\partial f/\partial y)^2\sigma_y^2$ [e.g., *Bevington and Robinson*, 1992]):

$$\sigma^2_{\text{geom.cal}}(l, k; \rho_{\text{meas}}) = \frac{\sigma^2_{\text{cam}}(l, k; \rho_{\text{meas}})}{\rho^2_{\text{meas}}(l, \text{nadir})} + \frac{\sigma^2_{\text{cam}}(l, \text{nadir}; \rho_{\text{meas}})\rho^2_{\text{meas}}(l, k)}{\rho^4_{\text{meas}}(l, \text{nadir})}, \quad (8b)$$

$\sigma_{\text{cam}}(l, k; \rho_{\text{meas}})$ is the contribution of band l, view angle k to the angle-to-angle relative calibration reflectance uncertainty, and is given by

$$\sigma^2_{\text{cam}} = \rho^2_{\text{meas}}[(\text{SNR}_{am}(l, k; \rho_{\text{meas}}))^{-2}], \tag{8c}$$

where unlike (7b), only the SNR is involved. Systematic angle-to-angle uncertainties are ignored, since for AirMISR, a single pivoting camera provides all the angular views. (For MISR, nine separate cameras cover the range of view angles, so angle-to-angle systematic uncertainties must be considered.) Value $\sigma^2_{\text{geom.var}}(l, k)$ is the variance of the equivalent reflectance ratio $[\rho_j(l, k)/\rho_j(l, \text{nadir})]$, calculated over all the pixels (indexed by j) in a patch.

$$\sigma^2_{\text{geom.var}}(l, k) = \frac{1}{M}\sum_j \left[\frac{\rho_{\text{meas}}(j; l, k)}{\rho_{\text{meas}}(j; l, \text{nadir})} - \left\langle \frac{\rho_{\text{meas}}(l, k)}{\rho_{\text{meas}}(l, \text{nadir})}\right\rangle\right]^2, \tag{8d}$$

$\sigma^2_{\text{geom.var}}$ falls between 10^{-2} and 10^{-3} for the cases considered in this study.

We define a spectral χ^2 in a way similar to χ^2_{geom}:

$$\chi^2_{\text{spec}} = \frac{1}{N\langle w_k\rangle}\sum_{\substack{k=1\\ l=4 \text{ only}}}^{9} \frac{w_k\left[\frac{\rho_{\text{meas}}(l, k)}{\rho_{\text{meas}}(\text{band3}, k)} - \frac{\rho_{\text{comp}}(l, k)}{\rho_{\text{comp}}(\text{band3}, k)}\right]^2}{(\sigma^2_{\text{spec.cal}}(l, k; \rho_{\text{meas}}) + \sigma^2_{\text{spec.var}}(l, k))} \tag{9a}$$

with

$$\sigma^2_{\text{spec.cal}}(l, k; \rho_{\text{meas}}) = \frac{\sigma^2_{\text{band}}(l, k; \rho_{\text{meas}})}{\rho^2_{\text{meas}}(\text{band3}, k)} + \frac{\sigma^2_{\text{band}}(\text{band3}, k; \rho_{\text{meas}})\rho^2_{\text{meas}}(l, k)}{\rho^4_{\text{meas}}(\text{band3}, k)}, \tag{9b}$$

and $\sigma_{\text{band}}(l, k; \rho_{\text{meas}})$ as the contribution of (band l, view angle k) to the band-to-band relative calibration reflectance uncertainty:

$$\sigma^2_{\text{band}} = \rho^2_{\text{meas}}[(\varepsilon_{\text{band\_sys}}(l, k; \rho_{\text{meas}})/100)^2 + (\text{SNR}_{am}(l, k; \rho_{\text{meas}}))^{-2}]; \tag{9c}$$

$\varepsilon_{\text{band\_sys}}$ is the uncertainty due to systematic factors in band-to-band calibration, expressed as a percent; its value is assessed at 0.7 for all cases, based on the calibration error budget [*Bruegge et al*., 1998b]; and $\sigma^2_{\text{spec.var}}(l, k)$ is the variance of the equivalent reflectance ratio $[\rho_j(l, k)/\rho_j(\text{band3}, k)]$, calculated over all the pixels (indexed by j) in a patch. Value $\sigma^2_{\text{spec.var}}$ falls between 10^{-4} and 10^{-5} for the cases considered in this study.

For each model-measurement comparison the variable χ^2_{max} is set equal to whichever of the three χ^2 test variables has the largest value. This is the most stringent test for that case, the one that determines whether the comparison model is rejected or accepted as representative of the observations.

We include a maximum deviation test variable that is the single largest term contributing to χ^2_{abs} (see equation (7a)):

$$\chi^2_{\text{max\_dev}} = \underset{l, k}{\text{Max}} \frac{[\rho_{\text{meas}}(l, k) - \rho_{\text{comp}}(l, k)]^2}{(\sigma^2_{\text{abs.cal}}(l, k; \rho_{\text{meas}}) + \sigma^2_{\text{abs.var}}(l, k))}. \tag{10}$$

All the other test variables are averages of up to 18 measurements. $\chi^2_{\text{max\_dev}}$ makes the greatest use of any band-specific or scattering-angle-specific phenomenon, such as a rainbow or a spectral absorption feature, in discriminating between measurements and comparison models. Since $\chi^2_{\text{max\_dev}}$ is skewed to higher values than the other three test variables, it cannot be evaluated on the same scale. We set a threshold for $\chi^2_{\text{max\_dev}}$ of 20 for accepting any model but do not use it in calculating χ^2_{max}.

The quantities $\varepsilon_{\text{abs\_sys}}$, $\varepsilon_{\text{band\_sys}}$, and SNR_{am} are stored in the AirMISR L1B2 product, as part of the grid metadata. They are called abs_rad_unc_sys, band_to_band_rel_unc_sys, and snr_4×4 (for the 4 × 4 averaging mode), respectively. These quantities are reported for each band and view angle, and at 15 equivalent reflectance values, which are listed in a vector called equiv_reflect in the grid metadata. Although the values of both ε variables are independent of band, view angle, and measured equivalent reflectance in the early calibration budget assessment, SNR_{am} must be interpolated to the appropriate equivalent reflectance (ρ_{meas}), as indicated in (7)–(10). Subsequent recalibrations may introduce equivalent reflectance dependence in the ε variables as well.

3.3. Interpretation of Test Variable Results

We have defined four dependent variables to be used in comparing measurements with models (χ^2_{abs}, χ^2_{geom}, χ^2_{spec}, and $\chi^2_{\text{max dev}}$). Since each χ^2 variable is normalized to the number of channels used, they are "reduced" χ^2 quantities. Formally, $\chi^2 < 1$ means that the average difference between the measured and the comparison quantities is less than the associated measurement error. A value less than or about unity implies that the comparison model is indistinguishable from the measurements. Values larger than about 5 imply that the comparison model is not likely to be consistent with the observations.

In the present analysis of AirMISR data, minimum values of χ^2_{max} fall between 3 and 4, slightly higher than the values of 1 to 2 found in purely theoretical sensitivity studies [*Kahn et al*., 1997, 1998, 2000]. The sensitivity studies used simulated "measurements," obtained from the same algorithm that produced the comparison model radiance, so it was possible to obtain exact matches. With real data, there are differences between the measured and the comparison model radiance patterns from unmodeled (and unknown) aspects of the environment, such as subpixel variability in atmospheric and surface properties. Since values of σ^2_{abs} are of the order of 10^{-7}, the test variable values of 3 to 4 that we obtain with real data amount to an average difference of a few percent between measured and comparison model equivalent reflectances. These are small enough to indicate we have a reasonable understanding of the measurement error that forms the denominators of χ^2 statistics. A quantitative assessment of subpixel scene variability, which makes the largest contribution to the measurement uncertainty in this case, is part of future field campaign plans for MISR.

4. Generic Aerosol Retrievals

The generic aerosol retrieval determines the range of column-average, cross-section-weighted mean aerosol populations that produce top-of-atmosphere radiances closest to the MISR or AirMISR measurements, as assessed by the χ^2 test variables [*Kahn et al*., 1998]. We assume a spherical, unimodal, lognormal size distribution of particles with uniform composition, and step through comparison models covering ranges of aerosol column optical depth (τ_c), column number-mean aerosol characteristic radius (r_c), and column mean real and

Table 4. Parameter Space of Comparison Model Properties Used for the Generic Retrieval

	Minimum Value	Maximum Value	Number of Divisions
Aerosol optical depth at 0.56 μm	0.00	1.00	21
Characteristic radius	0.05	2.00	40
Real index of refraction	1.33	1.55	12
Imaginary index of refraction[a]	0.0	0.50	20

[a]Logarithmic scale used.

imaginary indices of refraction (nr_c, ni_c). Table 4 gives the four-dimensional parameter space of comparison model properties selected. The widths of the particle size distributions were fixed at 2.51.

We ran nine cases for each patch. The nominal case uses the mean equivalent reflectances over the patch (Table 3). To provide a crude assessment of confidence in the solutions, we also ran the algorithm with all the equivalent reflectances set to mean + standard deviation (the "mean +" cases), and to mean − standard deviation (the "mean −" cases). For these three sets of equivalent reflectances, we assumed near-surface wind speed for the comparison model space to be 0.0, 2.5, or 5.0 m s^{-1}. According to the Monterey Bay Aquarium Research Institute M1 buoy, which operated at the time of the AirMISR flight (Figure 1), near-surface winds in the vicinity of the observed location fell between 5 and 10 knots (about 2.5 to 5.0 m s^{-1}), closer to the low end of this range.

Figure 5 is a scatterplot matrix of the generic retrieval results for Run 1, Patch 1 of the June 29 Monterey data, using the mean AirMISR equivalent reflectances and assumed 2.5 m s^{-1} near-surface wind speed. Each of the four independent comparison model aerosol variables, τ_c, r_c, nr_c, and ni_c, is represented by one row and one column in this figure. Each off-diagonal graph is a scatterplot showing values of two variables for models that meet a $\chi^2_{\max}$ criterion, when compared with the AirMISR measurements. For a given scatterplot, all values of the two aerosol variables not displayed are included in the search for cases that meet the criterion (i.e., this is a projection of the four-dimensional space onto two dimensions, not a 2-D section of the 4-D space). Different symbols are used for cases that meet several ranges of $\chi^2_{\max}$ criteria, starting with $\chi^2_{\max} < 3.25$. This figure provides both the range of each comparison model variable that meets each criterion and the correlations among variables that meet the criteria. A tabulation of the key results for all nine equivalent reflectance and assumed wind speed cases is given in Table 5.

Solutions for the smallest $\chi^2_{\max}$ have values of aerosol column optical depth in Band 2 (τ_a) tightly constrained around 0.05. For r_a the range of cases covered in Table 5 spans values between 0.25 and 0.45 μm. (The subscript "a" is for "atmosphere.") The imaginary index of refraction ni_a has a preferred value of 0.0 for the nominal case, and solutions for all cases fall at the low end of the parameter space (Table 5). Systematic increases in ni_a follow increases in the assumed wind speed. By assuming more reflection from the surface due to whitecaps, high wind speed retrievals drive particle absorption (ni_a) to larger values. Similarly, by setting a low value for the observed reflectance, the "mean −" retrievals require larger ni_a as well. For $\chi^2_{\max} < 4$, nr_a is at the high end of the parameter space, between 1.51 and 1.55, but loosening the $\chi^2_{\max}$ criterion results in no significant constraint on nr_a for most cases, as would be expected on the basis of our generic retrieval sensitivity studies [*Kahn et al*., 1998].

The area around Run 1 Patch 1 contains the highest quality data of the Monterey experiment, i.e., most uniform and unaffected by Sun glint. We performed generic retrievals on three additional patches in the immediate vicinity of Patch 1, each centered 50–60 pixels (about 1.5 km) away, to the east, west, and north. The results for all these additional patches are indistinguishable from those for Patch 1. These results included all nine look angles.

We also analyzed Run 1 Patch 1 with the An (nadir) look angle masked out. The An view might be slightly contaminated with Sun glint, as indicated by the relatively small Sun glint angle ζ (Table 2) and possibly by the higher reflectance standard deviation for An (Table 3). However, eliminating the An camera measurements produces essentially the same results as the nine-angle analyses. Because of the varying air mass factor, we expect the steepest angles ("C" and "D") to provide the tightest constraints on aerosol properties; elimination of the An look angle does not have much effect on the result.

For Run 1 Patch 2, ζ for the Af, An, and Aa look angles are small enough to be considered for possible Sun glint contamination (Table 2). Supporting this observation, the An view shown in Figure 2 appears to brighten as one moves from Patch 1, where ζ is about 43°, to Patch 2, where ζ is less than 25°. The ζ below which a view is actually contaminated depends on near-surface wind speed and the relative azimuths of the Sun, wind, and look angle; the true wind vector is not well known in this case. However, a better indication of Sun glint effects is provided by the combination of relatively small ζ and relatively large reflectance variability on 30 m length scales. The standard deviation of equivalent reflectances for the An look angle exceeds those of all other look angles by an order of magnitude or more, and those for Af are about a factor of 2 higher than the remaining views (Table 3).

We applied the generic retrieval to the Run 1 Patch 2 data with the An and Af look angles masked out, and we experimented with masking out Aa as well. We also replaced the nadir reflectances with those from the Ba look angle for the normalization in (8a) and (8b). Regardless of these choices, the results are similar to those for Run 1 Patch 1. In terms of the reflectances the main difference from Run 1 Patch 1 is that the Ca and Da look angles are of the order of 10% brighter in the red and NIR channels of Patch 2. Accordingly, the optical depth solutions cover the same range as for Patch 1 but are skewed about 0.05 higher (Table 5). As with Patch 1, ni_a increases when the assumed surface wind speed is raised; and since two look angles are masked out, there is less overall constraint for Patch 2, so the minimum values of $\chi^2_{\max}$ are lower in some cases.

AirMISR flew directly toward the Sun on Run 2; view angles Cf, Bf, Af, An, and possibly Df are contaminated by Sun glint, based on the data in Tables 2 and 3. With four or five view angles contaminated, results are less meaningful than those for Run 1. When the Cf, Bf, Af, and An view angles are masked out, the minimum $\chi^2_{\max}$ values are still nearly 3 times larger than those for Run 1 Patch 1, due to poor matches with the Df view angle data. However, best solutions still produce optical depths between 0.05 and 0.15, and effective radii and refractive indices that also fall within the range obtained for Run 1 Patch 1 (Table 5).

The steep "D" angles are most effective at constraining

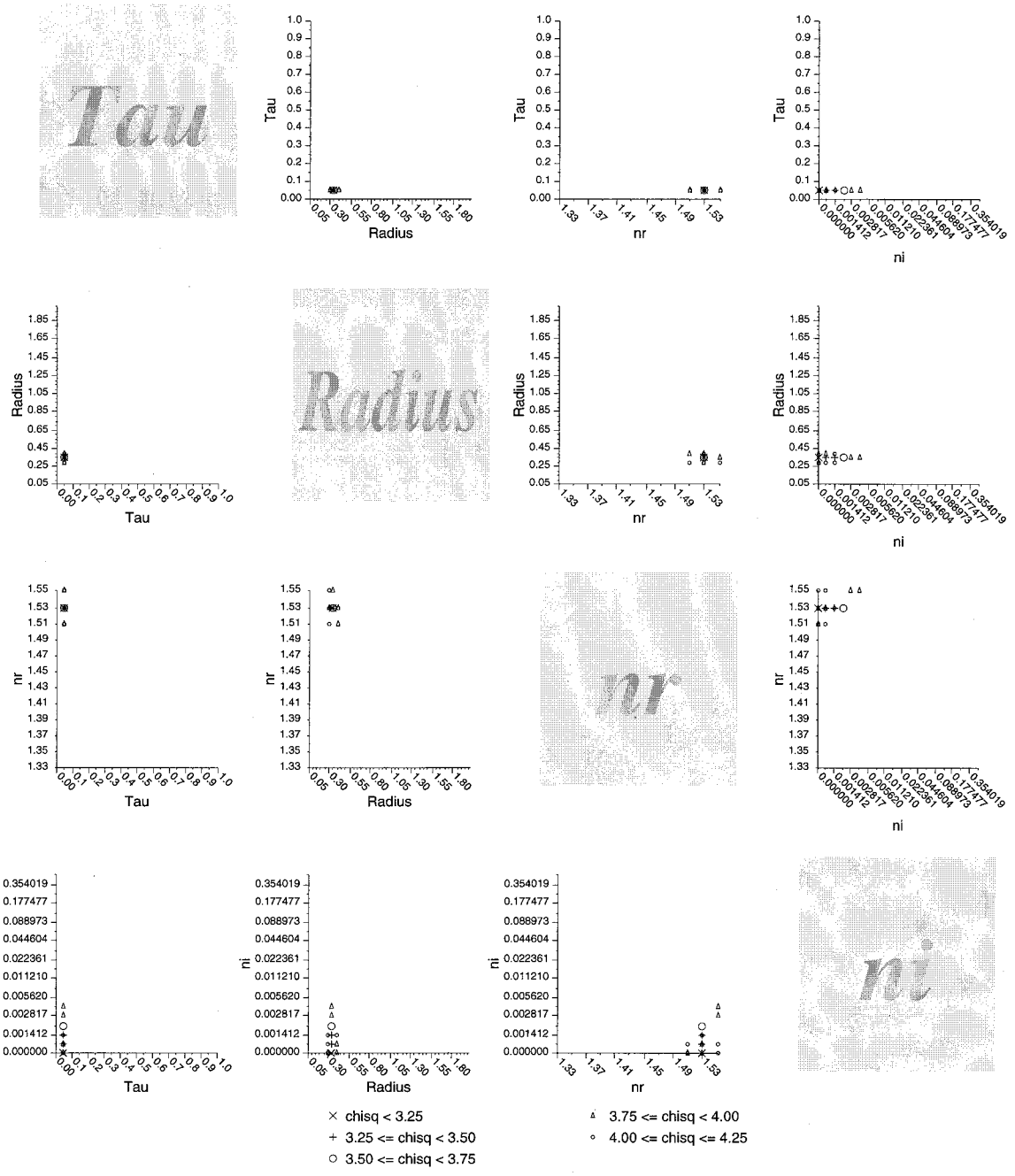

Figure 5. Generic aerosol retrieval scatterplot matrix for Run 1 Patch 1 of the AirMISR Monterey flight, June 29, 1999. Each of the four independent comparison model aerosol variables, τ_c, r_c, nr_c, ni_c, is represented by one row and one column, labeled "tau," "radius," "nr," and "ni," respectively. Note that ni is on a logarithmic scale; all others are linear. Each off-diagonal graph is a scatterplot showing values of two variables for comparison models that meet a $\chi^2_{\max}$ criterion, when compared with the AirMISR measurements. For a given scatterplot all values of the two aerosol variables not shown are included in the search for cases that meet the criterion. The figure legend identifies the $\chi^2_{\max}$ criterion corresponding to each symbol. Shown here is the case for mean equivalent reflectance values (Table 3) and an assumed near-surface wind speed of 2.5 m s^{-1}. Other cases are summarized in Table 5.

atmospheric properties, so when the Df view for Run 2 Patch 1 is masked out along with Cf, Bf, Af, and An, minimum $\chi^2_{\max}$ values are lowered, and the solution space expands. Because of the viewing geometry, the scene appears bright relative to the Run 1 patches, and with the reduced set of constraints, larger optical depths are obtained (Table 5). To keep the variation in equivalent reflectance from increasing too much as one views at steeper angles, larger imaginary refractive indices go along with the higher optical depths. Solutions having the lowest $\chi^2_{\max}$ are found when either the near-surface wind speed is assumed to be high (which makes the comparison model reflectances higher for a given aerosol optical depth) or the equivalent reflectances themselves are set artificially low.

In summary, we identified views showing aerosol and Sun

Table 5. Generic Retrieval Results, Monterey Bay[a]

Case	Wind Speed, m/s	Lowest χ^2_{max}	For Lowest χ^2_{max}				$\chi^2_{max} < 4$			
			τ_a	r_a	nr_a	ni_a	τ_a	r_a	nr_a	ni_a
Run 1 Patch 1										
Mean	0.0	2.99	0.05	0.35	1.53	0.00	0.05	0.30–0.40	1.51–1.55	0.00–0.004
Mean	2.5	3.12	0.05	0.35	1.53	0.00	0.05	0.35–0.40	1.51–1.55	0.00–0.004
Mean	5.0	3.25	0.05	0.30	1.53	0.002	0.05–0.15	0.25–0.45	*	0.00–0.022
Mean +	0.0	3.65	0.05	0.35	1.53	0.00	0.05	0.35–0.40	1.53	0.00
Mean +	2.5	3.86	0.05	0.35	1.53	0.00	0.05	0.35	1.53	0.00
Mean +	5.0	3.62	0.05	0.30	1.53	0.00	0.05–0.10	0.30–0.35	1.37–1.55	0.00–0.011
Mean −	0.0	2.60	0.05	0.35	1.51	0.00	0.05	0.30–0.45	1.51–1.55	0.00–0.008
Mean −	2.5	2.56	0.05	0.30	1.53	0.002	0.05–0.10	0.30–0.45	1.37–1.55	0.00–0.011
Mean −	5.0	2.83	0.10	0.35	1.37	0.008	0.05–0.20	0.25–0.45	*	0.00–0.031
Run 1 Patch 2 With An and Af Masked Out										
Mean	0.0	1.19	0.15	0.30	1.35	0.011	0.05–0.20	0.15–0.55	*	0.00–0.063
Mean	2.5	1.42	0.10	0.20	1.51	0.032	0.05–0.20	0.15–0.55	*	0.00–0.063
Mean	5.0	6.13	0.15	0.10	1.51	0.126	⋯	⋯	⋯	⋯
Mean +	0.0	1.20	0.15	0.30	1.33	0.011	0.10–0.20	0.15–0.55	*	0.00–0.045
Mean +	2.5	1.35	0.10	0.30	1.41	0.008	0.10–0.20	0.15–0.45	*	0.00–0.045
Mean +	5.0	5.85	0.15	0.10	1.51	0.126	⋯	⋯	⋯	⋯
Mean −	0.0	1.23	0.10	0.50	1.33	0.00	0.05–0.20	0.15–0.55	*	0.00–0.063
Mean −	2.5	1.39	0.10	0.30	1.41	0.011	0.05–0.20	0.15–0.55	*	0.00–0.63
Mean −	5.0	6.65	0.15	0.10	1.49	0.126	⋯	⋯	⋯	⋯
Run 2 Patch 1 With Cf, Bf, Af, and An Masked Out										
Mean	0.0	14.14	0.10	0.30	1.41	0.006	⋯	⋯	⋯	⋯
Mean	2.5	8.76	0.10	0.30	1.41	0.004	⋯	⋯	⋯	⋯
Mean	5.0	9.80	0.05	0.30	1.51	0.00	⋯	⋯	⋯	⋯
Mean +	0.0	20.18	0.15	0.30	1.41	0.022	⋯	⋯	⋯	⋯
Mean +	2.5	10.67	0.10	0.30	1.39	0.00	⋯	⋯	⋯	⋯
Mean +	5.0	10.02	0.05	0.30	1.51	0.00	⋯	⋯	⋯	⋯
Mean −	0.0	8.25	0.10	0.30	1.41	0.006	⋯	⋯	⋯	⋯
Mean −	2.5	9.71	0.10	0.30	1.41	0.006	⋯	⋯	⋯	⋯
Mean −	5.0	10.19	0.05	0.30	1.51	0.001	⋯	⋯	⋯	⋯
Run 2 Patch 1 With Df, Cf, Bf, Af, and An Masked Out										
Mean	0.0	3.76	0.35	0.25	1.33	0.022	⋯	⋯	⋯	⋯
Mean	2.5	2.35	0.30	0.20	1.39	0.032	0.20–0.35	0.15–0.25	1.33–1.47	0.008–0.045
Mean	5.0	1.31	0.25	0.20	1.43	0.032	0.20–0.35	0.10–0.25	*	0.006–0.063
Mean +	0.0	7.06	0.40	0.20	1.37	0.045	⋯	⋯	⋯	⋯
Mean +	2.5	3.88	0.35	0.25	1.33	0.022	⋯	⋯	⋯	⋯
Mean +	5.0	0.95	0.25	0.15	1.51	0.045	0.20–0.35	0.10–0.30	*	0.008–0.063
Mean −	0.0	1.21	0.30	0.20	1.39	0.032	0.20–0.40	0.15–0.25	1.33–1.53	0.011–0.063
Mean −	2.5	1.12	0.25	0.15	1.49	0.045	0.20–0.35	0.10–0.25	*	0.008–0.063
Mean −	5.0	1.60	0.20	0.15	1.55	0.045	0.15–0.30	0.10–0.25	*	0.008–0.063

[a]"Case" indicates whether the retrieval was performed on the mean equivalent reflectance values, the (mean + standard deviation) values, or the (mean − standard deviation) values (Table 3). "Wind speed" is the assumed near-surface wind speed. Columns 4–7 are retrieved aerosol properties at the lowest χ^2_{max} value, and columns 8–11 are the ranges of retrieved aerosol properties for $\chi^2_{max} < 4$. "Three center dots" indicate that no solutions were found, whereas "asterisks" indicate that solutions meeting the criterion covered the entire range within the parameter space (Table 4). For Run 1 Patch 2, Ba look angle reflectances are used for normalization.

glint in the AirMISR Monterey data. On the basis of the generic retrieval in the uncontaminated region, τ_a is between 0.05 and 0.10 in Band 2, with a preference for values on the low side of that range. Retrieved r_a is between 0.25 and 0.45 μm, with a preference for the 0.30–0.40 μm subrange, $ni_a < 0.004$, with 0.0 as the most likely value, and nr_a could be anywhere in the range 1.33–1.55, with a possible preference for 1.51–1.55. These properties correspond to a "medium-to-large, spherical" column-average, cross-section-weighted mean particle. An analysis of the measurements in terms of climatologically probable particle mixtures is given in section 5.

5. Climatological Aerosol Retrievals

The climatological aerosol retrieval asks what ranges of assumed, climatologically likely, external mixtures of component aerosols match the MISR or AirMISR measurements, as assessed by the χ^2 test variables [*Kahn et al.*, 2000]. This approach allows us to distinguish, as much as possible, air masses containing common mixtures of aerosols, to monitor their evolution, and to compare retrieval results with in situ observations and with aerosol transport model predictions.

The value of a climatological retrieval rests on the quality of the assumed climatology. Most satellite climatological retrievals currently used assume either one or two component aerosols. We adopt the global aerosol climatology developed by *Kahn et al.* [2000]. It is based on the results of monthly, global aerosol transport models for six component aerosols (summarized by *Tegen et al.* [1997]), interpolated to a 1° by 1° grid. From the six component aerosols, it is possible to select up to 15 combinations of four components. However, *Kahn et al.* [2000] found that only five combinations are needed to classify the four most abundant components in the transport model

Table 6. Climatological Mixing Groups[a]

Mixing Group	Classification	Component 1	Component 2	Component 3	Component 4
1	Carbonaceous + dusty maritime	sulfate	sea salt	carbonaceous	accum. dust
2	Dusty maritime + coarse dust	sulfate	sea salt	accum. dust	coarse dust
3	Carbonaceous + black carbon maritime	sulfate	sea salt	carbonaceous	black carbon
4	Carbonaceous + dusty continental	sulfate	accum. dust	coarse dust	carbonaceous
5	Carbonaceous + black carbon continental	sulfate	accum. dust	carbonaceous	black carbon
1C	Cirrus + carbonaceous maritime	sulfate	sea salt	carbonaceous	cirrus
2C	Cirrus + dusty maritime	sulfate	sea salt	accum. dust	cirrus
3C	Cirrus + black carbon maritime	sulfate	sea salt	black carbon	cirrus
4C	Cirrus + carbonaceous continental	sulfate	accum. dust	carbonaceous	cirrus
5C	Cirrus + dusty continental	sulfate	accum. dust	coarse dust	cirrus
6C	Cirrus + black carbon continental	sulfate	accum. dust	black carbon	cirrus

[a]"Accum. dust" stands for accumulation mode dust. Part of this table is abstracted from Table 2 of *Kahn et al*. [2000].

results. These five "mixing groups," listed in Table 6, form the comparison space we use for the AirMISR climatological retrieval.

We allow each of the four components in each mixing group to contribute a fraction of the total optical depth varying from zero to 1, in steps of 0.05. This creates 1771 comparison models covering all the fractional combinations of four components in a mixing group. To this we add comparison model optical depth in MISR Band 2 (τ_c) as another dimension, ranging from zero to 1 in 0.05 steps. Thus the space of comparison models contains five mixing groups, 1771 fractional combinations per mixing group, at 21 optical depth steps, for a total of 185,955 models.

To complete the comparison models, we must provide, in addition to the mixture component fractions, microphysical properties for each component aerosol. This is the most difficult part of the climatology to specify, since aerosol properties vary on many spatial and temporal scales. However, we expect MISR to make about a dozen distinctions based on particle microphysical properties, under good observing conditions [*Kahn et al*., 1998]. At this level of detail, MISR will be insensitive to fine distinctions in component aerosol size or composition, and in the absence of in situ measurements to provide additional constraints, we select commonly cited properties of broad particle classes.

Such microphysical properties for the six components, plus cirrus, were abstracted from standard references and are given in Table 7. (Phase functions for these particles are given by *Kahn et al*. [2000], Figure 1.) Note that in continental aerosol mixing groups (defined in Table 6), accumulation mode sulfate particles are hydrated to equilibrium at 70% relative humidity, and accumulation mode dust particles are assumed to be in the surface layer. For maritime aerosol mixing groups, accumulation mode sulfate particles are hydrated to 80% relative humidity, and accumulation mode dust particles are assumed to be in a layer 5–10 km above the surface, mixed with a scale height of 10 km. Column 10 in Table 7 refers to the qualitative classification of components based on MISR sensitivities [*Kahn et al*., 1998, 2000]; sizes are designated small, medium, or large, and shapes are spherical or randomly oriented nonspherical. The component microphysical properties assumed in this climatology will be reevaluated in light of retrieval results and in consideration of any field data available for a site of interest.

As with the generic retrieval, we ran nine cases for each patch, covering mean and perturbed equivalent reflectances as well as assumed near-surface wind speeds of 0, 2.5, and 5 m s^{-1}. Figure 6 is a whisker plot matrix that summarizes the results of the climatological retrieval using mean equivalent reflectances for Run 1, Patch 1 of the AirMISR Monterey flight, and assumed wind speed of 2.5 m s^{-1}. Each of the five rows of plots corresponds to comparisons made between the AirMISR data and the models from one of the five mixing groups. The columns correspond to different choices of comparison model optical depth. The horizontal axis for each whisker plot allows six positions, for each of the six pure particle types in this study. The vertical axis shows the range of fractional optical depth from zero to 1. There are no more than four whiskers in each plot, corresponding to the components of the relevant mixing group. Each whisker indicates the largest and smallest fractional optical depth of that component particle, for any comparison model in the mixing group that meets the criterion $\chi^2_{\max} < 4$. Longer whiskers indicate that comparison models meeting this criterion span a wider range of fractional optical depth. Note that correlations among components are not shown in Figure 6. However, an "x" on each whisker

Table 7. Component Aerosol Properties Assumed for Climatology[a]

Aerosol Type	r_1, μm	r_2, μm	r_c, μm	σ	n_r (MISR Band)	n_i (MISR Band)	ω_0, 672 nm	RH, %	Particle Size/Shape Category
Sulfate (accum.) over land	(0.007) 0.007	(0.7) 0.81	(0.07) 0.08	(1.86) 1.88	(1.53) 1.46	0.0 (all)	1.0	(0) 70	medium spherical
Sulfate (accum.) over ocean	(0.007) 0.008	(0.7) 1.05	(0.07) 0.10	(1.86) 1.87	(1.53) 1.39	0.0 (all)	1.0	(0) 80	medium spherical
Sea salt (accum.)	(0.05) 0.098	(1.0) 1.98	(0.35) 0.61	(2.51) 2.29	(1.50) 1.35	0.0 (all)	1.0	(0) 80	large spherical
Mineral dust[b] (accum.)	0.05	2.0	0.47	2.60	1.53	0.0085 (1) 0.0055 (2) 0.0045 (3) 0.0012 (4)	0.91	···	medium nonspherical
Mineral dust[b] (coarse)	0.5	15.0	1.90	2.60	1.53	0.0085 (1) 0.0055 (2) 0.0045 (3) 0.0012 (4)	0.73	···	large nonspherical
Carbonaceous[c]	0.007	2.0	0.13	1.80	1.50	0.025 (all)	0.87	97	medium spherical
Black carbon	0.001	0.5	0.012	2.00	1.75	0.455 (1) 0.440 (2) 0.435 (3) 0.430 (4)	0.17	···	small
Thin cirrus[d]	3.0	200.	···	···	1.316 (1) 1.311 (2) 1.308 (3) 1.304 (4)	0.0 (all)	1.0	100	very large fractal

[a]This table is taken from Table 3 of *Kahn et al*. [2000]; r_1 and r_2 are the lower and upper radius limits for the particle size distribution. "Accum." stands for "accumulation mode" particles. Particle number concentrations are distributed lognormally, with characteristic radius r_c and width σ; ω_0 is the single-scattering albedo, given here at the effective wavelength of the MISR red channel. RH is the relative humidity to which hygroscopic particles are hydrated. Sulfate and sea-salt particles are hydrated to the RH value in the "RH" column using the model of *Hanel* [1976]; where properties for these particle types are in parentheses, they refer to the dry particles. The aerosol physical data are abstracted from *Shettle and Fenn* [1979], *d'Almeida et al*. [1991], *World Climate Program* (*WCP*) [1984], and other sources, except as indicated. Optical data for spherical particles are calculated using standard Mie theory.

[b]Nonspherical (randomly oriented mixed spheroid) mineral dust models based on *Mishchenko et al*. [1997].

[c]Carbonaceous particle model based on *Reid et al*. [1998].

[d]Fractal thin cirrus model based on *Mishchenko et al*. [1996].

indicates the component fractional optical depth for the comparison model in the relevant mixing group with the lowest value of $\chi^2_{\max}$.

In Figure 6, only models in mixing group 3 meet the criterion, and then only for $\tau_c = 0.1$. This is a Maritime air mass, and the predominant component is sea salt, the large, spherical, nonabsorbing particle in the climatology. It accounts for about 50% of the total optical depth in this retrieval. About 30–40% is assigned to sulfate and/or carbonaceous components, which are medium, spherical particles that are nonabsorbing and slightly absorbing, respectively. This result supports the sensitivity study conclusion that it would be difficult to distinguish sulfate from carbonaceous components with multiangle data [*Kahn et al*., 2000]. The remaining 15% to 25% is attributed to black carbon, a small, absorbing particle.

Results for other mixing groups that meet a looser criterion, $\chi^2_{\max} < 8$, are still all maritime, having roughly 50% sea salt, 40% sulfate + carbonaceous particles, and 10% of a more absorbing aerosol, either black carbon or accumulation mode dust, though black carbon is favored over the nonspherical dust particles. Similarly, Run 1 Patch 1 cases having perturbed equivalent reflectances and/or off-nominal assumed surface wind speeds return only maritime air masses composed primarily of sea salt and sulfate + carbonaceous particles, and optical depth 0.10 or 0.15. We expect an accuracy of ±15–20% for component particle optical depth observed over dark water in the climatological retrievals, based on sensitivity study results [*Kahn et al*., 2000]. Thus the climatological and generic retrievals provide complementary results, and a consistent picture of aerosol properties emerges from the Monterey data.

Figure 7 illustrates the solution space for six mixing groups that include thin cirrus, as defined in Table 6. This figure also shows the effect of loosening the acceptance criterion to $\chi^2_{\max} < 8$. Only maritime air masses meet the criterion, and except for cases with unreasonably large fractions of black carbon, which are rejected on physical grounds [see *Kahn et al*., 2000], only models having optical depth 0.10. Of the remaining models the best solutions contain about 50% sea salt, 30–50% sulfate + carbonaceous, and the remainder, black carbon. Air masses containing significant fractions of nonspherical particles, either mineral dust or cirrus, are rejected by the climatological retrieval; and when the acceptance criterion is set to $\chi^2_{\max} < 4$, the solution space is a subset of that covered in Figure 7, limited to cirrus mixing group 3, optical depth 0.10, in accord with the results of Figure 6.

6. Discussion and Conclusions

The generic and climatological retrievals for the June 29, 1999, Monterey AirMISR observations, in the region uncontaminated by Sun glint, give complementary results. The generic retrieval searches thoroughly a four-dimensional, mono-

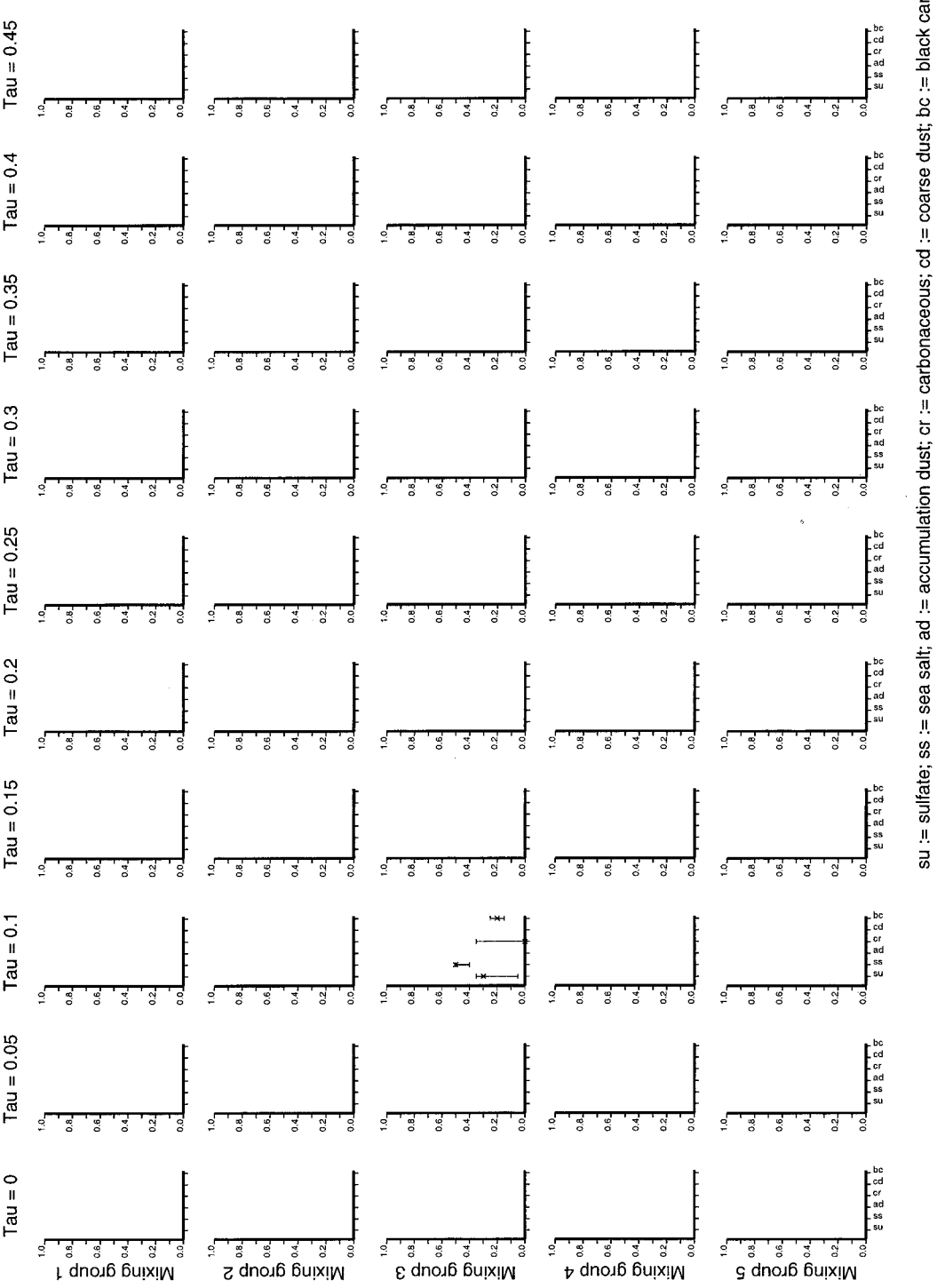

Figure 6. Whisker plot matrix summarizing climatological retrieval results using mean equivalent reflectances for Run 1 Patch 1 of the AirMISR Monterey flight and assumed wind speed of 2.5 m s^{-1}. The five rows show comparisons between the data and each of the five noncirrus mixing groups in Table 6. Each column contains plots for one choice of comparison model optical depth. The horizontal axis in each plot allows six positions for whiskers, one for each component in the climatology (Table 7). The vertical axes indicate the fraction of column optical depth in MISR Band 2 contributed by a particle type. Each plot summarizes the comparisons between the AirMISR data and all 1771 comparison models in one mixing group and optical depth. Whiskers are drawn spanning the upper and lower limits of fractional contribution of each component in the mixing group, for any model that meets the criterion $\chi^2_{max} < 4$. Fractions of component particle contributions for the comparison model yielding the smallest value of χ^2_{max} are marked by a "cross" on each whisker.

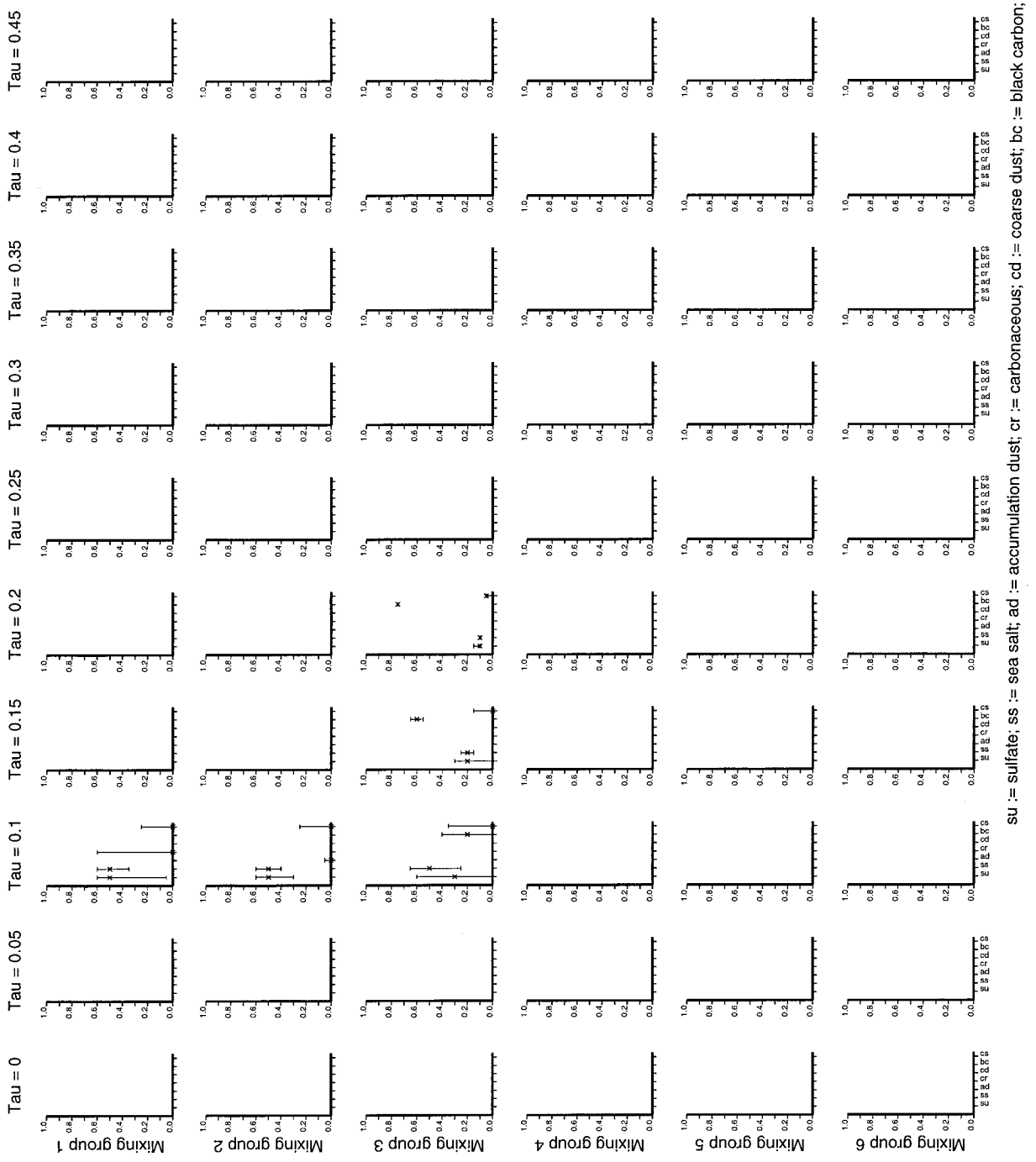

Figure 7. Whisker plot matrix similar to Figure 6, also for the nominal case of Run 1 Patch 1, but for cirrus mixing groups defined in Table 6, and using the looser acceptance criterion $\chi^2_{\max} < 8$.

modal aerosol comparison space of spherical particles, in the current implementation. Within the limits of an assumed climatology the climatological retrieval identifies air mass types that match the observations, composed of up to four component aerosols.

On the basis of the generic retrieval the cross-section-weighted, column-mean aerosol properties are as follows: τ_a between 0.05 and 0.10, with a preference for values on the low side of the range, r_a between 0.25 and 0.45 μm, with a preference for the 0.30–0.40 μm subrange, and $ni_a < 0.004$, with 0.0 as the most likely value. These properties correspond most closely to a "medium-to-large, spherical" column-average particle.

The climatological retrieval identifies a maritime air mass, containing no nonspherical particles such as mineral dust. To an accuracy of about ±15% the retrieved mixing ratio of sea salt (large, spherical, nonabsorbing particles) is 50% in MISR Band 2 and 40% for the sulfate + carbonaceous (medium, spherical) components. In agreement with the generic results, the column optical depth comes to about 0.1.

We also found that over dark water, pixel-to-pixel scene variability can contribute more to the retrieval uncertainty than camera calibration, requiring us to add σ_{var} terms to the χ^2 definitions (equations (7a), (8a), and (9a)), which did not appear in previous theoretical sensitivity studies. In accord with the theoretical studies, (1) sensitivity to optical depth at middle-visible wavelengths is of the order of 0.05, (2) medium, spherical, nonabsorbing particles (the assumed "sulfate" component) is not easily distinguished from medium, spherical, somewhat absorbing "carbonaceous" particles, but (3) spherical particles are easily distinguished from randomly oriented nonspherical ones. High spatial variance of the reflectance, in addition to geometric considerations, proved to be a better indicator of Sun glint contamination than geometry alone.

Some limited, near-coincident data were acquired from other sources. It may be compared with the following AirMISR results:

1. According to general circulation model back trajectories [*HYSPLIT*, 1999], the near-surface air at Monterey Bay in the late morning of June 29, 1999, spent at least the previous five days over the north central Pacific Ocean. Higher-level air (300 HPa) originated in the subtropical east Pacific. Such histories would produce a maritime air mass, as observed.

2. The MISR validation team deployed several instruments at the Marina site, just onshore near the AirMISR Run 2 flight line on June 29 (Figure 1). They report an aerosol optical depth of 0.096 at 519.9 nm, 1802 UTC, which remained within 10% of that value for the subsequent hour, based on Reagan Sun photometer measurements [*MISR Validation Team*, 1999]. At 1805 UTC, data from the team's Multifilter Rotating Shadowband Radiometer (MFRSR) at the site produced aerosol optical depths of 0.091 at 615.5 nm and 0.109 at 499.6 nm. Preliminary analysis of CIMEL Sun photometer and MFRSR data taken between 1812 and 1818 UTC identifies a peak in the number density of particles at effective radius ~0.5 μm, superimposed on a power-law background distribution over accumulation mode sizes (S. Pilorz, personal communication, 2000). These values compare well with the AirMISR results.

3. About 45 km southeast of the AirMISR nadir-looking image centers, the Center for Interdisciplinary Remotely Piloted Aircraft Studies (CIRPAS) Twin Otter [*Bluth et al*., 1995], carrying University of Washington instruments, flew two vertical profiles during the AirMISR runs. A preliminary report by S. Gassó identifies a marine-type aerosol and total column optical depth at 550 nm around 0.08, consistent with the other observations. More detailed composition and size distribution data from this experiment will be forthcoming.

The current MISR aerosol climatology [*Kahn et al*., 2000], derived from transport model results [*Tegen et al*., 1997], reports the carbonaceous + dusty maritime mixing group for September through March for the Monterey area. On a monthly average, the expected air mass contains a sea-salt component having a mixing ratio of about 10% and more than 70% sulfate + carbonaceous components; the rest is accumulation mode dust. For June and July the climatology for Monterey identifies the carbonaceous + dusty continental mixing group, which does not contain a significant fraction of sea salt but does contain in excess of 30% mineral dust, an amount easily precluded by the AirMISR analysis. The predicted total aerosol optical depth in middle-visible wavelengths is between about 0.07 and 0.12, in accord with the observations.

One of the goals of the MISR mission is to add spatial detail and information about temporal variability to the global aerosol climatology. The analysis of AirMISR data, given in this paper, is an early step toward this goal. It is illustrated by the consistency of the climatological and generic retrieval results, the agreement of these with the limited constraints from other sources, and the discrepancy in aerosol air-mass-type between the climatological retrieval and the transport model prediction.

Detailed, coincident field measurements, lacking in this case, are needed to better constrain algorithm sensitivities to particle properties and cirrus and to quantify the effect of subpixel variation on the measurement uncertainty. These are the subjects of the continuing MISR aerosol retrieval validation program.

Acknowledgments. We thank Carol Bruegge, James Conel, David Diner, Barbara Gaitley, Mark Helmlinger, William Ledeboer, Roger Marchand, and Stu Pilorz, all members of the MISR Validation team, for helping provide the AirMISR data and the MISR field data used in this study. Santiago Gassó and Dean Hegg reported their Monterey aircraft results in advance of publication. We thank Carol Bruegge, David Diner, Barbara Gaitley, Santiago Gassó, Veljko Jovanovic, William Ledeboer, and Stu Pilorz for valuable discussions about this work. The Monterey Bay Aquarium Research Institute provided wind speed data from their M1 buoy. This research is supported by the EOS-MISR instrument program and by the Climate and Radiation Research and Analysis Program in the Earth Sciences Division of the National Aeronautics and Space Administration, under R. Curran. This work was performed at the Jet Propulsion Laboratory, California Institute of Technology, under contract with NASA.

References

Abdou, W. A., J. V. Martonchik, R. Kahn, R. West, and D. Diner, A modified linear-mixing method for calculating atmospheric path radiances of aerosol mixtures, *J. Geophys. Res*., *102*, 16,883–16,888, 1997.

Bevington, P. R., and D. K. Robinson, *Data Reduction and Error Analysis for the Physical Sciences*, 2nd ed., pp. 328, McGraw-Hill, New York, 1992.

Bluth, R. T., P. A. Durkee, J. H. Seinfeld, R. C. Flagan, and L. M. Russell, The Center for Interdisciplinary Remotely Piloted Aircraft Studies (CIRPAS), *Bull. Am. Meteorol. Soc*., *77*, 2691–2699, 1995.

Bruegge, C. J., V. G. Duval, N. L. Chrien, R. P. Korechoff, B. J. Gaitley, and E. B. Hochberg, MISR prelaunch instrument calibration and characterization results, *IEEE Trans. Geosci. Remote Sens*., *36*, 1186–1198, 1998a.

Bruegge, C. J., N. Chrien, D. Diner, R. Kahn, and J. Martonchik, MISR radiometric uncertainty analyses and their utilization within geophysical retrievals, *Metrologia*, *35*, 571–579, 1998b.

Bruegge, C. J., N. L. Chrien, and D. J. Diner, MISR Level 1 in-flight radiometric calibration and characterization algorithm theoretical basis, *JPL D-13398, Rev. A*, Jet Propul. Lab., Pasadena, Calif., 1999a.

Bruegge, C. J., D. J. Diner, R. P. Korechoff, and M. Lee, MISR Level 1 radiance scaling and conditioning algorithm theoretical basis, *JPL D-11507, Rev. E*, Jet Propul. Lab., Pasadena, Calif., 1999b.

Chrien, N. L., C. J. Bruegge, and B. J. Gaitley, AirMISR laboratory calibration and in-flight performance results, *Remote Sens. Environ*., in press, 1999.

Cox, C., and W. Munk, Statistics of the sea surface derived from Sun glitter, *J. Mar. Res*., *13*, 198–227, 1954.

d'Almeida, G. A., P. Koepke, and E. P. Shettle, *Atmospheric Aerosols: Global Climatology and Radiative Characteristics*, A. Deepak, Hampton, Va., 1991.

Diner, D. J., et al., Multiangle Imaging SpectroRadiometer (MISR) description and experiment overview, *IEEE Trans. Geosci. Remote Sens*., *36*, 1072–1087, 1998a.

Diner, D. J., et al., The Airborne Multi-angle Imaging SpectroRadiometer (AirMISR): Instrument description and first results, *IEEE Trans. Geosci. Remote Sens*., *36*, 1339–1349, 1998b.

Diner, D. J., et al., MISR level 2 aerosol retrieval algorithm theoretical basis, *JPL D11400, Rev. D*, Jet Propul. Lab., Pasadena, Calif., 1999a.

Diner, D. J., W. A. Abdou, H. R. Gordon, R. A. Kahn, Y. Knyazikhin, J. V. Martonchik, D. McDonald, S. McMuldroch, R. Myneni, and R. A. West, MISR level 2 ancillary products and data sets algorithm theoretical basis, *JPL D-13402, Rev. B*, Jet Propul. Lab., Pasadena, Calif., 1999b.

Grant, I. P., and G. E. Hunt, Solution of radiative transfer problems using invariant S_n method, *Mon. Not. R. Astron. Soc*., *141*, 27–41, 1968.

Hanel, G., The properties of atmospheric aerosol particles as functions of relative humidity at thermodynamic equilibrium with the surrounding moist air, *Adv. Geophys*., *19*, 73–188, 1976.

Hybrid Single-Particle Lagrangian Integrated Trajectory (HYSPLIT4), Model, *http://www.arl.noaa.gov/ready/hysplit4.html*, NOAA Air Resour. Lab., Silver Spring, Md., 1999.

Jovanovic, V. M., M. M. Smyth, J. Zong, R. Ando, and G. W. Bothwell, MISR photogrammetric data reduction for geophysical retrievals, *IEEE Trans. Geosci. Remote Sens*., *36*, 1290–1301, 1998.

Kahn, R., R. West, D. McDonald, B. Rheingans, and M. I. Mishchenko, Sensitivity of multiangle remote sensing observations to aerosol sphericity, *J. Geophys. Res*., *102*, 16,861–16,870, 1997.

Kahn, R., P. Banerjee, D. McDonald, and D. Diner, Sensitivity of Multiangle imaging to aerosol optical depth, and to pure-particle size distribution and composition over ocean, *J. Geophys. Res*., *103*, 32,195–32,213, 1998.

Kahn, R., P. Banerjee, and D. McDonald, Sensitivity of multiangle imaging to natural mixtures of aerosols over ocean, *J. Geophys. Res*., in press, 2000.

Koepke, P., Effective reflectance of oceanic whitecaps, *Appl. Opt*., *23*, 1816–1824, 1984.

Martonchik, J. V., D. J. Diner, R. Kahn, M. M. Verstraete, B. Pinty, H. R. Gordon, and T. P. Ackerman, Techniques for the retrieval of aerosol properties over land and ocean using multiangle imaging, *IEEE Trans. Geosci. Remote Sens*., *36*, 1212–1227, 1998.

Mishchenko, M. I., and L. D. Travis, Satellite retrieval of aerosol properties over the ocean using polarization as well as intensity of reflected sunlight, *J. Geophys. Res*., *102*, 16,989–17,013, 1997.

Mishchenko, M. I., W. B. Rossow, A. Macke, and A. A. Lacis, Sensitivity of cirrus cloud albedo, bidirectional reflectance and optical thickness retrieval accuracy to ice particle shape, *J. Geophys. Res*., *101*, 16,973–16,985, 1996.

Mishchenko, M. I., L. Travis, R. Kahn, and R. West, Modeling phase functions for dust-like tropospheric aerosols using a shape mixture of randomly oriented polydisperse spheroids, *J. Geophys. Res*., *102*, 16,831–16,847, 1997.

MISR Validation Team, CIMEL data, MFRSR data, Reagan Sun photometer data, *http://www-misr.jpl.nasa.gov/mission/valwork/mivalres.html*, NASA, 1999.

Monahan, E. C., and I. O. Muircheartaigh, Optimal power-law description of oceanic whitecap coverage dependence on wind speed, *J. Phys. Oceanogr*., *10*, 2094–2099, 1980.

Reid, J. S., P. V. Hobbs, R. J. Ferek, D. R. Blake, J. V. Martins, M. R. Dunlap, and C. Liousse, Physical, chemical, and optical properties of regional hazes dominated by smoke in Brazil, *J. Geophys. Res*., *103*, 32,059–32,080, 1998.

Shettle, E. P., and R. W. Fenn, Models for the aerosols of the lower atmosphere and the effects of humidity variations on their optical properties, *AFGL-TR-79-0214*, 94 pp., Air Force Geophys. Lab., Bedford, Mass., 1979.

Stowe, L. L., A. M. Ignatov, and R. R. Singh, Development, validation, and potential enhancements to the second-generation operational aerosol product at the National Environmental Satellite, Data, and Information Service of the National Oceanic and Atmospheric Administration, *J. Geophys. Res*., *102*, 16,923–16,934, 1997.

Tegen, I., P. Hollrig, M. Chin, I. Fung, D. Jacob, and J. Penner, Contribution of different aerosol species to the global aerosol extinction optical thickness: Estimates from model results, *J. Geophys. Res*., *102*, 23,895–23,915, 1997.

Tsang, L., J. A. Kong, and R. T. Shin, *Theory of Microwave Remote Sensing*, 613 pp., John Wiley, New York, 1985.

Wang, M., and H. R. Gordon, Estimating aerosol optical properties over the oceans with the multiangle imaging spectroradiometer: Some preliminary results, *Appl. Opt*., *33*, 4042–4057, 1994.

World Climate Programme, A preliminary cloudless standard atmosphere for radiation computation, WCP-112, 53 pp., Int. Assoc. for Meteorol. and Atmos. Phys., Boulder, Colo., 1984.

P. Banerjee, R. Kahn, J. Martonchik, and D. McDonald, Jet Propulsion Laboratory, California Institute of Technology, 4800 Oak Grove Drive, Pasadena, CA 91109. (ralph.kahn@jpl.nasa.gov)

(Received June 13, 2000; revised October 10, 2000;
accepted November 6, 2000.)